Environment International 213 (2026) 110340

Contents lists available at ScienceDirect

Environment International

journal homepage: www.elsevier.com/locate/envint

Full length article

Contrasting aerosol regimes and radiative forcing across the Andean–Amazonian transition: A seven-year analysis of biomass burning impacts

Cesar Victoria-Barros [a,*], René Estevan [b], Octavio Fashé Raymundo [a], Héctor Navarro-Barboza [c]

[a] Facultad de Ciencias Físicas, Universidad Nacional Mayor de San Marcos, Av. Carlos Germán Amezaga N° 375, Lima, 15001, Peru
[b] Instituto Geofisico del Perú, Calle Badajoz Mz.Ñ Lt 08 y 09, Urb. Mayorazgo 4ta Etapa - Ate, Lima, 15012, Peru
[c] Universitat Politècnica de Catalunya · BarcelonaTech (UPC), C/ Colom, 11, Ed. TR5, 08222 Terrassa (Barcelona), Spain

ARTICLE INFO

Dataset link: https://aeronet.gsfc.nasa.gov/, https://firms.modaps.eosdis.nasa.gov/, https://disc.gsfc.nasa.gov/, https://www.ready.noaa.gov/, https://www.ready.noaa.gov/HYSPLIT.php, https://paulricchiazzi.com/www/sbdart/

Keywords:
Biomass burning
Aerosol composition
Radiative forcing
Backward trajectories
South American aerosols

ABSTRACT

Biomass burning in the Amazon Basin is a major source of atmospheric aerosols affecting regional climate and air quality across tropical South America, yet the contrasting impacts on high-altitude Andean and lowland Amazonian environments remain poorly quantified. Here we present a seven-year (2015–2021) integrated analysis of aerosol transport pathways, composition, and radiative forcing at two contrasting receptor sites: Huancayo Observatory (3313 m a.s.l.) in the Peruvian Andes and Rio Branco (212 m a.s.l.) in the southwestern Brazilian Amazon. By combining AERONET Level 2.0 observations, HYSPLIT backward trajectories, VIIRS-SNPP active fire detections, and MERRA-2 speciated aerosol products, we identify two fundamentally distinct aerosol regimes within the same regional system. Rio Branco experiences direct, near-field exposure (<200 km) to intense biomass burning during June–October, with extreme aerosol loading (AOD_{440} up to 1.25; $PM_{2.5}$ exceeding 50 μg m^{-3}), pronounced organic carbon dominance (>90% of $PM_{2.5}$), and atmospheric radiative forcing of +75 W m^{-2} during the SON peak—among the highest reported for Amazonian biomass-burning conditions. In contrast, Huancayo receives diluted, aged smoke via long-range transport (300–600 km), with mixed composition including persistent mineral dust (18%–30%) and sulfate (12%–23%), and a substantially lower atmospheric forcing of +33 W m^{-2}. The resulting 2.3-fold inter-site difference in atmospheric radiative forcing, robust within an SSA-perturbation uncertainty envelope, illustrates how source proximity and topographic barriers jointly modulate aerosol–climate interactions across the Andean–Amazonian transition zone, with implications for regional circulation, precipitation feedbacks, and Andean cryosphere stability.

1. Introduction

Aerosol radiative forcing represents a critical yet highly uncertain component of Earth's climate system, with direct effects ranging from −0.5 to −1.0 W m^{-2} globally, comparable in magnitude but opposite in sign to CO_2 forcing (Legg, 2021). Unlike well-mixed greenhouse gases, aerosols exhibit extreme spatiotemporal variability driven by heterogeneous emission sources, short atmospheric lifetimes (days to weeks), and complex interactions with radiation and clouds (Myhre et al., 2013). Biomass burning (BB) aerosols are particularly important in tropical regions, where they simultaneously scatter incoming solar radiation (cooling effect) and absorb radiation through black and brown carbon (warming effect), creating strong vertical heating gradients that can alter atmospheric stability, cloud formation, and regional circulation patterns (Li et al., 2022; Navarro-Barboza et al., 2025).

Global assessments of aerosol radiative forcing have advanced significantly through integrated observational networks and modeling frameworks, yet profound regional disparities persist. In Europe and North America, dense ground-based networks (AERONET, GAW) coupled with satellite retrievals have enabled comprehensive characterization of aerosol optical properties and radiative effects across industrial, agricultural, and wildfire-influenced regions (Palacios-Peña et al., 2019; Ma and Yu, 2014). Asian megacities have received intensive scrutiny through field campaigns such as ABC-EAREX, quantifying strong atmospheric heating (+10 to +30 W m^{-2}) from absorbing aerosols over densely populated regions (Nakajima et al., 2007). In

* Corresponding author.
E-mail address: cesar.victoria@unmsm.edu.pe (C. Victoria-Barros).

https://doi.org/10.1016/j.envint.2026.110340
Received 18 February 2026; Received in revised form 11 May 2026; Accepted 28 May 2026
Available online 6 June 2026

contrast, tropical South America – home to the world's largest BB emissions during the austral dry season – remains critically underrepresented in global radiative forcing assessments. While studies across the Amazon Basin have documented elevated aerosol optical depth during fire seasons (Sena et al., 2012, 2013), they mostly focus on optical properties rather than radiative forcing quantification. Furthermore, the role of topographic barriers in modulating aerosol transport and composition between lowland source regions and high-altitude receptor sites remains poorly constrained, limiting our understanding of aerosol–climate impacts across the Andean–Amazonian transition zone.

Established methodological tools in trajectory modeling, combined with long-term ground-based observations provide opportunities to address these knowledge gaps. The Hybrid Single-Particle Lagrangian Integrated Trajectory model (HYSPLIT; (Draxler and Hess, 1998)) enables quantitative assessment of aerosol transport pathways and source attribution, while AERONET (Holben et al., 1998; Giles et al., 2019) provides standardized, quality-assured aerosol optical properties essential for radiative forcing calculations. Previous studies at Huancayo Observatory in the Peruvian Andes identified maximum AOD during September coinciding with Amazonian fire peaks (Estevan et al., 2019; Navarro-Barboza et al., 2020; Victoria and Estevan, 2021; Victoria-Barros and Estevan Arredondo, 2025), suggesting long-range transport of BB aerosols across the eastern cordillera. At Rio Branco in the southwestern Amazon, Pérez-Ramírez et al. (2017) reported elevated AOD and Ångström exponent values with single scattering albedo ranging from 0.93 to 0.95 depending on fire intensity, indicating substantial absorption by fresh combustion aerosols. However, these studies analyzed sites independently without comparative assessment of transport mechanisms, composition differences, or contrasting radiative impacts between lowland source regions and high-altitude receptor sites.

This study addresses these gaps through integrated analysis of aerosol transport, composition, optical properties, and radiative forcing at two contrasting sites over seven years (2015–2021): Huancayo Observatory (3313 m a.s.l.) in the central Peruvian Andes and Rio Branco (212 m a.s.l.) in the Brazilian Amazon. Building upon the methodological framework established in Victoria-Barros and Estevan Arredondo (2025) for the single-site analysis at Huancayo (which used the same seven-year AERONET dataset, HYSPLIT backward-trajectory clustering, and SBDART radiative transfer approach), the present work extends and refines that framework through the systematic comparative analysis with Rio Branco as a contrasting lowland Amazonian receptor site. We combine AERONET Level 2.0 observations, HYSPLIT backward trajectory analysis using GDAS meteorological fields, VIIRS-SNPP active fire detections (replacing the lower-resolution MODIS product), and MERRA-2 speciated aerosol products to: (1) characterize dominant transport pathways and their intersection with fire source regions; (2) quantify seasonal variations in aerosol composition and size distributions; (3) assess aerosol optical properties including single scattering albedo and asymmetry parameter; and (4) calculate direct aerosol radiative forcing at surface, top-of-atmosphere, and within the atmospheric column. Methodological refinements relative to the previous Huancayo-only analysis include the introduction of a trajectory-weighted fire index (Section 3.1.2) and a formal MERRA-2 vs. AERONET AOD validation (Section 2.2.3). To our knowledge, this represents the first systematic intercomparison of aerosol regimes across the Andean–Amazonian transition zone, quantifying for the first time the inter-site differences in radiative forcing driven by source proximity and topographic barriers in this vulnerable tropical region.

The paper is organized as follows: Section 2 describes the study sites and datasets; Section 3 details the methodological framework; Section 4 presents the results and their discussion; and Section 5 summarizes the main findings.

2. Study area and data sources

2.1. Study area

This research focuses on two contrasting receptor sites in tropical South America (Fig. 1): Huancayo Observatory in the central Peruvian Andes and Rio Branco in the southwestern Brazilian Amazon, representing distinct topographic and environmental settings across the Andean–Amazonian transition zone.

Huancayo (12.04° S, 75.32° W, 3313 m a.s.l.) is situated in the Mantaro River valley within an intermontane depression between the Western and Eastern Cordilleras of the central Andes (Uribe-Ventura et al., 2025). With a population of approximately 400,000 inhabitants, the city experiences a subtropical highland climate with distinct wet (October–April) and dry (May–September) seasons. The high-altitude location isolates Huancayo from direct local emissions, making it an ideal receptor site for studying long-range aerosol transport from the Amazon Basin and regional dust sources from the Altiplano and inter-Andean valleys.

Rio Branco (9.96° S, 67.87° W, 212 m a.s.l.) is the capital of Acre state in northwestern Brazil, with a population of 419,452 (2021) representing approximately 43% of the state's population and 63% of the regional vehicle fleet (Coker et al., 2022). Embedded within the southwestern Amazon Basin, the city experiences a tropical monsoon climate with pronounced wet (November–March) and dry (June–September) seasons. During the dry season, the region is heavily impacted by BB from deforestation and agricultural fires, making it ideal for studying direct exposure to Amazonian fire emissions.

Both sites are equipped with AERONET sun photometer stations providing long-term aerosol optical depth and inversion products. The contrasting elevations, geographic settings, and distances from BB source regions enable comparative analysis of aerosol transport mechanisms, composition, and optical properties across the Andean–Amazonian system.

2.2. Data sources

2.2.1. Ground-based aerosol data

In this study, aerosol observations were obtained from the Aerosol Robotic Network (AERONET; (Holben et al., 1998; Giles et al., 2019)), a global ground-based remote-sensing network established by the National Aeronautics and Space Administration (NASA). AERONET consists of more than 200 stations worldwide and provides standardized, well-calibrated, and quality-assured measurements of aerosol optical, microphysical, and radiative properties, enabling consistent long-term monitoring (Sangura et al., 2025).

The AERONET stations at Huancayo and Rio Branco are equipped with CIMEL Electronique CE-318 sun–sky radiometers (field of view 1.2°). These instruments measure direct solar irradiance and diffuse sky radiance at temporal resolution of 15 min, covering spectral ranges of 340–1640 nm for direct sun observations and 440–1020 nm for sky radiance measurements (Sangura et al., 2025). The data and associated aerosol inversion products are publicly available through the official AERONET archive (http://aeronet.gsfc.nasa.gov).

We used AERONET Version 3.0 data with Level 2.0 quality assurance, which represents fully validated observations following rigorous cloud screening, calibration, and quality control procedures. Compared to earlier releases, Version 3.0 incorporates significant improvements in near-real-time quality control of aerosol optical depth (AOD) measurements and inversion algorithms (Dehkhoda et al., 2024). The corresponding Level 2.0 inversion products provide high-confidence aerosol optical parameters at multiple wavelengths. Only Version 3.0, Level 2.0 data were considered in this analysis to ensure the highest data quality and consistency.

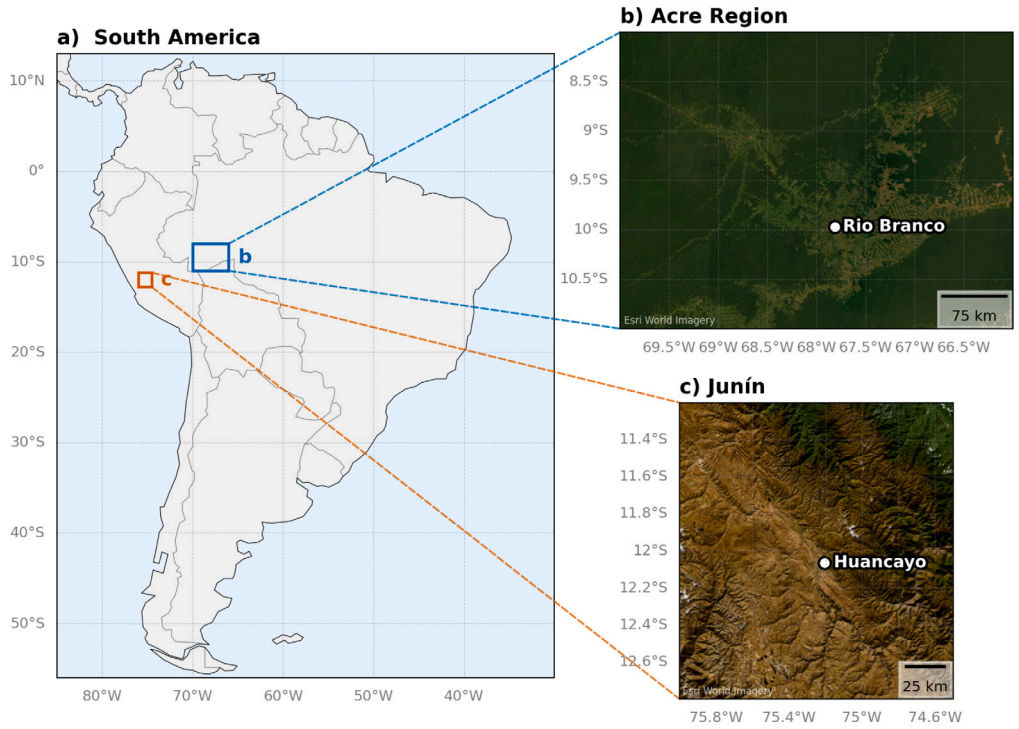

Fig. 1. Study region in tropical South America showing Huancayo Observatory, Peru and Rio Branco, Brazil. Topography illustrates the contrasting high-altitude Andean and lowland Amazonian settings.

2.2.2. Active fire detections

Fire activity was characterized using the Visible Infrared Imaging Radiometer Suite (VIIRS) aboard the Suomi National Polar-orbiting Partnership (VIIRS-SNPP, Schroeder et al. (2014)) satellite. VIIRS provides active fire detections with 375 m spatial resolution at nadir, significantly finer than the legacy MODIS 1 km product, enabling improved detection of small fires characteristic of deforestation and agricultural burning in tropical regions. Fire detections were obtained as CSV files aggregated by country and year for 2015–2021 from NASA's Fire Information for Resource Management System (FIRMS; https://firms.modaps.eosdis.nasa.gov/). Each detection includes geographic coordinates, fire radiative power (FRP, MW), confidence level, and acquisition time. We used only high-confidence detections to minimize false positives and calculated mean seasonal FRP density (MW km^{-2}) to characterize fire intensity across trajectory source regions.

2.2.3. MERRA-2 reanalysis products

Aerosol composition and $PM_{2.5}$ concentrations were obtained from the Modern-Era Retrospective Analysis for Research and Applications, Version 2 (MERRA-2; Gelaro et al. (2017), Randles et al. (2017)). MERRA-2 is produced by NASA's Global Modeling and Assimilation Office (GMAO) using the GEOS-5 (Goddard Earth Observing System) atmospheric model coupled with the GOCART (Goddard Chemistry Aerosol Radiation and Transport) aerosol module (Randles et al., 2017). The system provides daily speciated aerosol mass concentrations at $0.5° \times 0.625°$ horizontal resolution, assimilating Aerosol Optical Depth (AOD) retrievals from MODIS and MISR to constrain the total aerosol loading. The dataset was accessed through the NASA Goddard Earth Sciences Data and Information Services Center (GES DISC; https://disc.gsfc.nasa.gov/).

The reanalysis partitions total aerosol mass into five primary components: black carbon (BC), organic carbon (OC), dust, sulfate (SO_4^{2-}), and sea salt. It is important to clarify that while the total aerosol mass is constrained by the assimilation of observed AOD, the individual chemical speciation is determined by the GOCART model's internal physics and emission inventories (Randles et al., 2017). Consequently, the relative proportions of these species are model-derived estimates rather than direct observations.

To assess the reliability of these products at our study sites, MERRA-2 total AOD at 550 nm (TOTEXTTAU) was validated against collocated AERONET Level 2.0 observations (2015–2021). AERONET AOD was interpolated to 550 nm using the 440–870 nm Ångström exponent (Eck et al., 1999). The comparison yields robust Pearson correlation coefficients ($r = 0.715$ at Huancayo; $r = 0.936$ at Rio Branco) with an RMSE of 0.059 at both sites (Figure S1). The near-zero bias at Rio Branco (MBE = +0.004) confirms excellent performance in BB conditions. The modest positive bias at Huancayo (MBE = +0.041) is consistent with documented challenges of reanalysis products over complex Andean topography (Buchard et al., 2017).

We acknowledge the inherent uncertainty in aerosol speciation. However, the strong AOD agreement and the high correlations between MERRA-2 $PM_{2.5}$ and AERONET AOD_{440} during peak burning seasons (Rio Branco SON: $r = 0.93$; Huancayo JJA: $r = 0.83$, Table 3) indicate that the reanalysis effectively captures the dominant aerosol signals. To maintain methodological rigor, MERRA-2 data are used here exclusively for source attribution and compositional context, while all quantitative radiative forcing calculations rely solely on AERONET-retrieved optical properties.

2.2.4. Meteorological input

To perform the atmospheric transport simulations, this research utilizes the Global Data Assimilation System (GDAS1; (National Centers for Environmental Prediction, National Weather Service, NOAA, U.S. Department of Commerce, 2000)). GDAS1 is a global meteorological product generated by the National Centers for Environmental Prediction (NCEP) that integrates satellite, aircraft, and surface observations into a numerical weather prediction model.

The dataset provides gridded meteorological fields on a global scale with a horizontal resolution of $1° \times 1°$ (approximately 100 km × 100 km) and a temporal resolution of 3 h. While finer resolutions (such as 0.25°) are available, the 1° resolution is widely adopted for long-range

transport studies and HYSPLIT trajectories due to its computational efficiency and historical consistency (Faisal and Islam, 2026).

Vertically, the GDAS1 output used in this study includes 23 pressure levels, ranging from 1000 hPa (near surface) to 20 hPa (upper stratosphere). For each grid point, 32 atmospheric variables are provided, including key parameters for fire emission modeling such as:

- **Surface variables:** Surface pressure, 2-meter air temperature, 10-meter zonal (U) and meridional (V) wind components, and 6-hourly accumulated precipitation.
- **Profile variables:** Geopotential height, relative humidity, and temperature across the 23 vertical levels.

GDAS1 data are maintained and distributed by the National Oceanic and Atmospheric Administration (NOAA) and were retrieved from the Air Resources Laboratory (ARL) server (https://www.ready.noaa.gov/).

3. Methodology

3.1. Atmospheric transport and trajectory model

3.1.1. HYSPLIT model configuration

The Hybrid Single-Particle Lagrangian Integrated Trajectory (HYSPLIT) model (Stein et al., 2015) was employed to characterize atmospheric transport pathways and identify the origin of air masses reaching the study sites. HYSPLIT is a complete system for computing air parcel trajectories and complex dispersion simulations (Draxler and Hess, 1998), combining Lagrangian (moving frame of reference) and Eulerian (fixed grid) methodologies (Draxler and Spayd, 1999). Developed and maintained by NOAA's Air Resources Laboratory, HYSPLIT has become one of the most widely used atmospheric transport models in the atmospheric sciences community (Rolph et al., 2017), particularly for characterizing long-range transport of BB emissions (Freitas et al., 2005).

This approach is particularly relevant in South America, where persistent low-level jets and organized atmospheric circulation patterns transport BB aerosols from the Amazon basin across continental scales (Freitas et al., 2005; Marengo et al., 2004), significantly altering aerosol optical properties and radiative balance over the central Andes (Sena et al., 2012; Navarro-Barboza et al., 2020). HYSPLIT has been successfully applied in numerous regional studies examining BB transport (Mendez-Espinosa et al., 2019; Bolaño-Truyol et al., 2022; Rosas Santana et al., 2025), providing an established methodological framework for this research.

In this study, 120-hour (5-day) backward trajectories were computed to capture synoptic-scale transport from the main BB hotspots in the Amazon and Andean regions to the monitoring stations. This period is sufficient to encompass the typical transport timescales from major source regions while maintaining reasonable trajectory accuracy (Stohl, 1998; Draxler and Hess, 1998). Trajectories were initialized at 200 m above ground level (agl), approximately equivalent to 975 hPa at sea level or ~680 hPa at elevated sites such as Huancayo (3313 m a.s.l.). This height was selected to ensure sampling within the planetary boundary layer (PBL), where aerosols mix efficiently and are most likely to influence ground-level observations, while avoiding the immediate effects of local surface friction and topographic obstacles (Draxler and Spayd, 1999). The model was driven by GDAS meteorological fields at 1°×1° horizontal resolution with 3-hourly temporal resolution, providing adequate representation of synoptic-scale circulation patterns relevant to long-range aerosol transport.

Several limitations of the HYSPLIT approach merit explicit acknowledgment, particularly given the complex Andean topography at Huancayo. The GDAS1 meteorological fields at 1° × 1° resolution (~100 km) cannot resolve mesoscale orographic flows associated with the steep elevation gradients of the eastern Andean cordillera (lowlands at ~200 m to ridges >4,000 m over <100 km), nor sub-grid features such as valley channeling and orographic uplift. Trajectory positional uncertainty typically reaches 100–300 km after 5 days under synoptic conditions (Stohl, 1998; Draxler and Hess, 1998) and is likely amplified over complex terrain. In addition, HYSPLIT trajectories represent kinematic transport only, without aerosol deposition or chemical transformation, which is particularly relevant for the 300–600 km transport pathway to Huancayo. These limitations are inherent to Lagrangian trajectory analysis and should be considered when interpreting individual cluster characteristics, but the dominant transport patterns identified here are robust across multiple years and corroborated by independent AERONET and MERRA-2 observations and by the trajectory-weighted fire correlations (Section 3.1.2; Table 3).

3.1.2. Trajectory clustering analysis

To synthesize the large trajectory dataset into dominant transport patterns, a K-means clustering algorithm was applied following the methodology of Dorling et al. (1992). This multivariate statistical technique partitions trajectories into homogeneous groups by minimizing the within-cluster sum of squared Euclidean distances between trajectory endpoints. The algorithm iteratively assigns each trajectory to the nearest cluster centroid based on the geographical coordinates (latitude and longitude) of air parcel positions along the trajectory path, then recalculates centroids until convergence is achieved.

The optimal number of clusters was determined using the Total Spatial Variance (TSV) criterion (Kalkstein et al., 1987), which identifies the point where adding another cluster no longer produces a significant reduction in the total spatial variance of the dataset. Following this procedure, five clusters ($k = 5$) were selected for each site to balance meteorological diversity and interpretability while distinguishing between key source regions.

For each cluster, the mean trajectory and associated spatial variability were calculated. Residence time analysis was performed to identify preferential source regions by computing the total time air parcels spent over each grid cell during transport. These cluster-resolved transport patterns were then integrated with VIIRS-SNPP active fire detections (Schroeder et al., 2014) to link specific BB events with aerosol loading recorded at the AERONET stations.

To quantify the linkage between fire activity and aerosol loading along specific transport pathways, a trajectory-weighted fire index was developed. For each month m and receptor site, a ±1° geographic buffer was constructed around each of the five 120-h HYSPLIT cluster-mean backward trajectories. VIIRS-SNPP active-fire detections falling within each buffer during month m were identified via spatial indexing, and their total Fire Radiative Power (FRP, MW) was summed. The trajectory-weighted fire index was then computed as

$$F_{\text{weighted}}(m) = \sum_{k=1}^{5} w_k \cdot F_k(m), \tag{1}$$

where $F_k(m)$ is the total FRP within the buffer of cluster k during month m, and w_k is the fraction of backward trajectories assigned to cluster k in the corresponding season. This formulation filters out fire activity that does not contribute to aerosol transport toward the receptor site, directly linking the trajectory clustering analysis to the fire–aerosol correlations reported in Section 4.2 (Table 3).

The choice of a ±1° buffer (~110 km at the latitudes of the study sites) was guided by three considerations: (i) the typical positional uncertainty of HYSPLIT trajectories driven by GDAS1 meteorology at 1° resolution, which reaches 100–300 km after 5 days of integration (Stohl, 1998); (ii) consistency with the spatial resolution of the underlying meteorological field; and (iii) the typical horizontal scale of biomass-burning smoke plumes in the Amazon Basin (100–500 km) (Freitas et al., 2005; Artaxo et al., 2013). A sensitivity analysis using buffer widths of ±0.5°, ±1.0°, ±1.5°, and ±2.0° showed that the trajectory-weighted index consistently outperformed regional aggregation across all buffer sizes tested (Supplementary Material, Table S1), indicating that the improvement is driven by spatial filtering rather than by the specific buffer choice.

3.2. Aerosol radiative forcing estimation

Atmospheric aerosols modify the Earth's radiation budget by scattering and absorbing incoming shortwave solar radiation and, to a lesser extent, by absorbing and emitting longwave terrestrial radiation. The perturbation to the radiative energy balance caused by aerosols is quantified through Aerosol Radiative Forcing (ARF), defined as the change in net radiative flux due to the presence of aerosols (Boucher et al., 2013). Estimating ARF remains challenging due to the high spatial and temporal variability of aerosol properties, contributing significantly to uncertainties in climate assessments (Legg, 2021).

ARF is calculated at two atmospheric boundaries: the top of the atmosphere (TOA, typically at the tropopause or 100 km for radiative transfer models) and the bottom of the atmosphere (BOA, surface level). At the TOA, ARF represents the net radiative perturbation to the Earth–atmosphere system:

$$\Delta \mathrm{ARF}_{\mathrm{TOA}} = \left(F^{\downarrow}_{\mathrm{TOA}} - F^{\uparrow}_{\mathrm{TOA}}\right) - \left(F^{\downarrow}_{\mathrm{TOA},0} - F^{\uparrow}_{\mathrm{TOA},0}\right), \quad (2)$$

where $F^{\downarrow}_{\mathrm{TOA}}$ and $F^{\uparrow}_{\mathrm{TOA}}$ are the downward and upward radiative fluxes at the TOA with aerosols present, and $F^{\downarrow}_{\mathrm{TOA},0}$ and $F^{\uparrow}_{\mathrm{TOA},0}$ are the corresponding fluxes in aerosol-free conditions. All fluxes are expressed in W m^{-2}.

At the surface (BOA), ARF quantifies the change in net radiation available for surface processes:

$$\Delta \mathrm{ARF}_{\mathrm{BOA}} = \left(F^{\downarrow}_{\mathrm{BOA}} - F^{\uparrow}_{\mathrm{BOA}}\right) - \left(F^{\downarrow}_{\mathrm{BOA},0} - F^{\uparrow}_{\mathrm{BOA},0}\right), \quad (3)$$

where the subscripts follow the same convention as Eq. (2).

The atmospheric radiative forcing ($\Delta \mathrm{ARF}_{\mathrm{ATM}}$) represents the net absorption of radiative energy within the atmospheric column:

$$\Delta \mathrm{ARF}_{\mathrm{ATM}} = \Delta \mathrm{ARF}_{\mathrm{TOA}} - \Delta \mathrm{ARF}_{\mathrm{BOA}}. \quad (4)$$

A positive $\Delta \mathrm{ARF}_{\mathrm{ATM}}$ indicates atmospheric heating, while negative values indicate cooling. By convention, negative ARF values indicate a cooling effect (reduction in net downward flux), while positive values indicate warming.

3.2.1. SBDART radiative transfer model configuration

ARF was calculated using the Santa Barbara DISORT Atmospheric Radiative Transfer (SBDART; (Ricchiazzi et al., 1998)) model, a plane-parallel radiative transfer code that employs the discrete ordinates algorithm (Stamnes et al., 1988) to solve the radiative transfer equation in a vertically stratified atmosphere. For each AERONET Level 2.0 observation, SBDART was executed twice – once with observed aerosol properties and once under aerosol-free conditions – enabling direct quantification of aerosol radiative effects through flux differencing (Eqs. (2)–(4)).

The model was configured with the following specifications:

- **Spectral coverage:** Solar spectrum from 0.3 to 2.8 μm at 0.01 μm resolution, capturing > 90% of incoming solar radiation
- **Atmospheric profile:** Sub-arctic summer standard atmosphere (`idatm=6`) with site-specific surface pressure adjustment for Huancayo's elevation (3313 m a.s.l., `zpres=3.3`)
- **Surface albedo:** Six-band vegetation model (`isalb=6`) representative of tropical forest (Rio Branco) and highland grassland (Huancayo)
- **Solar geometry:** Observation-specific solar zenith angles computed from AERONET date, time, and geographic coordinates
- **Atmospheric composition:** Precipitable water vapor and total column ozone from AERONET; CO_2 fixed at 410 ppm (2015–2021 average)
- **Aerosol properties:** User-defined aerosol model (`iaer=5`) with AERONET-retrieved optical depth, single scattering albedo, and asymmetry parameter at four wavelengths (440, 675, 870, 10 20 nm). The aerosol vertical distribution follows SBDART's standard exponential tropospheric profile (approximately 2 km scale height) parameterized through the boundary-layer optical depth (`tbaer`, equal to the AERONET-retrieved AOD at 0.55 μm) and the Ångström exponent (`abaer`, $\alpha_{440-870}$), placing the bulk of aerosol mass within the planetary boundary layer and lower free troposphere (0–3 km). This is consistent with documented vertical distributions of BB aerosols in tropical South America (Ricchiazzi et al., 1998).
- **Output:** Upward and downward radiative fluxes at surface (0 km) and top of atmosphere (100 km)

Two methodological aspects warrant clarification. All ARF calculations are based on cloud-free observations only, since AERONET Level 2.0 data incorporate rigorous cloud-screening algorithms (Giles et al., 2019); the reported values therefore represent *clear-sky direct aerosol radiative forcing*, the standard quantity in the AERONET-based BB literature (Sena et al., 2013; Rosas Santana et al., 2025). The exponential vertical profile assumption introduces ~5%–15% uncertainty in the within-atmosphere component (Sena et al., 2013; Rai et al., 2019), but the column-integrated optical depth is directly constrained by AERONET, ensuring that relative comparisons between sites remain robust.

The DISORT solver employed 16 computational streams, balancing accuracy and computational efficiency. This automated workflow processed thousands of AERONET observations spanning 2015–2021, yielding instantaneous ARF estimates for comprehensive seasonal and interannual analysis.

4. Results and discussion

This section presents the seasonal variability of aerosol properties and their radiative impacts at two contrasting receptor sites: Huancayo in Peru and Rio Branco in Brazil. We adopt Southern Hemisphere seasonal definitions: summer (December–February, DJF), autumn (March–May, MAM), winter (June–August, JJA), and spring (September–November, SON). The analysis follows a systematic progression from (1) atmospheric transport patterns and fire source regions; (2) temporal evolution of aerosol loading and composition; (3) aerosol size distributions and optical properties; to (4) quantification of direct aerosol radiative forcing at surface, top-of-atmosphere, and within the atmospheric column. This structure reveals how Amazonian BB emissions during the austral dry season (JJA–SON) drive fundamentally different aerosol regimes at the two sites, with profound implications for seasonal radiative forcing patterns and regional climate impacts across the Andean–Amazonian transition zone.

4.1. Atmospheric transport patterns

To identify the source regions of aerosols reaching the study sites, we analyzed 120-hour backward trajectories initialized at 200 m above ground level. The analysis reveals distinct transport regimes dominated by the contrasting topographies of the Andean highlands and the Amazonian lowlands.

At Huancayo, the transport patterns are heavily influenced by the complex Andean topography, which acts as a physical barrier to low-level moisture and aerosol transport from the Amazon Basin Estevan et al. (2019). Fig. 2 and Table 1 show that the seasonal cycle is dominated by a wet-vs-dry dichotomy. During the wet season (DJF–MAM), long-range easterly trajectories prevail (88.8% combined easterly contributions in DJF; 90.6% in MAM), traversing the Peruvian Amazon and Eastern Cordillera under active South American Summer Monsoon (SASM) circulation, with associated wet deposition efficiently scavenging aerosols before they reach the Andes (Navarro-Barboza et al., 2020). The dry season (JJA) is characterized by substantially shorter east-northeasterly trajectories (C2: 69.3%, ~113 km), reflecting weakened monsoonal forcing and increased atmospheric stability. Spring (SON) marks the SASM reactivation, with the dominant ESE pathway (C1: 67.3%) showing increased path lengths relative to JJA.

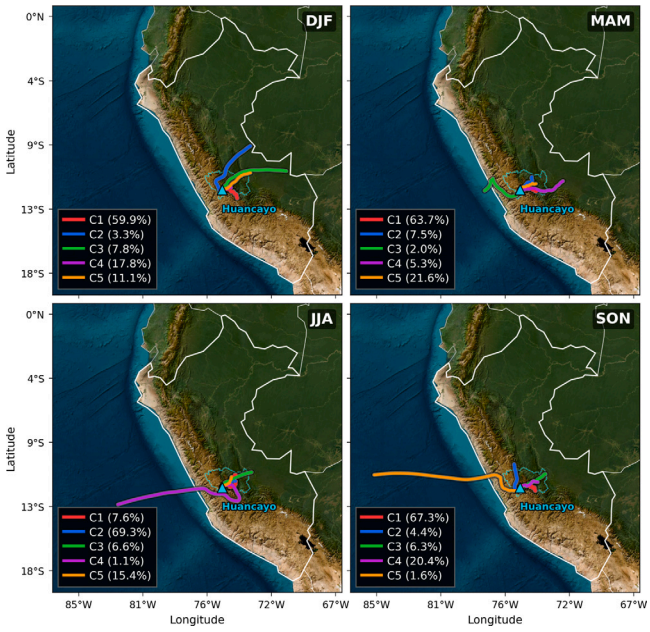

Fig. 2. Cluster analysis of backward trajectories for Huancayo (2015–2021). The 5-cluster solution highlights the variability in air mass origins reaching the central Andes across seasons (DJF, MAM, JJA, SON). Centroids (lines) illustrate the average path for each group, with the legend showing the contribution (%) of each cluster to the total transport.

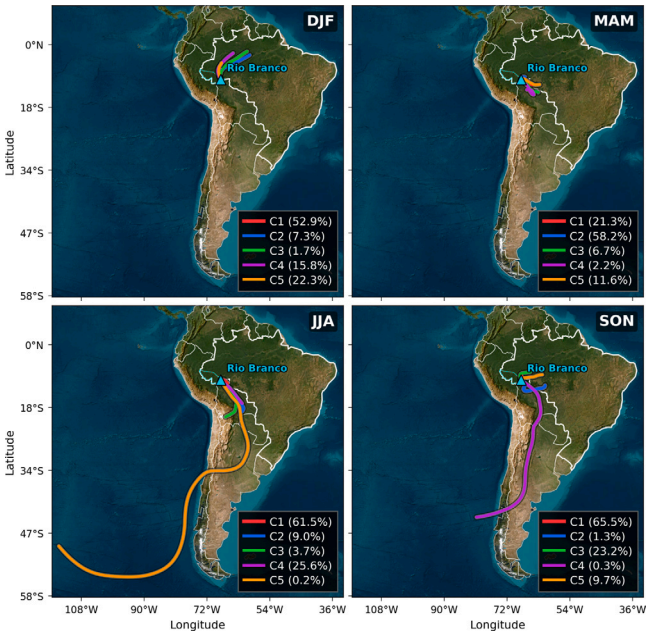

Fig. 3. Similar to Fig. 2, but for Rio Branco.

A distinctive feature of the dry-to-spring transition at Huancayo is the emergence of long-range Pacific westerly transport, entirely absent during summer. In JJA, C4 (1.1%) follows an anticyclonic loop originating from the southeastern Pacific (~800 km, W), crossing the western Cordillera and traversing the Altiplano. In SON, C5 (1.6%, W) extends even further west of 85°W (~1,114 km), representing the longest fetch distances observed across all seasons and potentially carrying marine aerosols, mineral dust from coastal regions, or long-range transported pollutants. Although these westerly clusters represent a very rare component of near-surface transport (1.1–1.6% of trajectories at 200 m AGL) and likely reflect mid-tropospheric flow rather than boundary-layer pathways, consistent with the prevalence of Pacific subsidence over the western Andean slopes during the austral dry season (Garreaud et al., 2009).

In contrast, Rio Branco exhibits short-range trajectories year-round, confined to the Amazon Basin (Fig. 3 and Table 1), with a clear seasonal shift in source direction. During DJF and SON, northern and northeastern pathways dominate (>85% combined), originating from the tropical Atlantic and northern Amazon Basin under monsoon-driven circulation. The MAM transition is dominated by a remarkably short ENE pathway (C2: 58.2%, ~149 km) reflecting reduced large-scale advection during the monsoon retreat, with southeastern trajectories collectively contributing ~42%. The dry season (JJA) shows a complete shift to southeastern air masses (C1: 61.5%, ESE; C4: 25.6%, SE; combined ~87%), originating from the immediate vicinity of Acre and Rondônia and directly intersecting the most intense BB regions. Minor southern long-range pathways (C3 in JJA, C4 in SON) account for <4% of trajectories but extend over ~1,000–4000 km, occasionally crossing northern Bolivian territory.

The contrasting transport regimes between the two sites reflect topographic control on atmospheric circulation. At Huancayo (3313 m a.s.l.), the Andes act as a dynamic barrier (Espinoza et al., 2015; Garreaud et al., 2009) producing seasonal dichotomy: long-range easterly trajectories during the wet season (>60%) versus substantially shorter trajectories during the dry season, plus the emergence of Pacific westerly components during winter–spring (1.1–1.6%). In contrast, Rio Branco (212 m a.s.l.) exhibits consistently short-range trajectories year-round, shifting seasonally from northern/northeastern sources (>85% in summer–spring) to southeastern sources (~87% in winter) (Moran-Zuloaga et al., 2018). While both sites experience SASM-related variability, Huancayo's trajectory lengths vary threefold seasonally and access mixed Amazonian–Pacific aerosol sources (marine aerosols, long-range pollutants, Altiplano dust), whereas Rio Branco remains dominated by regional Amazonian sources (biogenic emissions, BB, local anthropogenic) throughout the annual cycle (Moran-Zuloaga et al., 2018; Artaxo et al., 2013). These contrasting transport regimes set the stage for the analysis of fire-aerosol coupling that follows: the same trajectory pathways that distinguish the two sites also determine which fire source regions effectively contribute to aerosol loading at each receptor.

We additionally evaluated the sensitivity of the trajectory analysis to the receptor height by re-computing the full cluster solution with starting points at 500 m AGL (Supplementary Table S2 and Figures S2, S3). The dominant transport regimes are preserved at both sites: easterly/east-northeasterly transport remains the leading pathway at Huancayo across all seasons (44.6–67.5% at 500 m vs. 59.9–69.3% at 200 m), and the seasonal northern-to-southeastern shift at Rio Branco is also reproduced. We retain 200 m AGL as the primary receptor height in the main analysis to remain within the planetary boundary layer where AERONET column AOD and MERRA-2 surface $PM_{2.5}$ are most directly attributable to surface-level transport processes (Draxler and Spayd, 1999), while documenting the robustness of the main conclusions to this choice.

4.2. Wildfire activity and spatial distribution

Figs. 4 and 5 show the spatial distribution of mean Fire Radiative Power (FRP) density from VIIRS-SNPP active-fire detections (2015–2021) across the trajectory source regions reaching Huancayo and Rio Branco, respectively. Both sites exhibit pronounced seasonality, with FRP density ranging from near-zero during the wet season to exceeding 20 MW km^{-2} during the BB peak. The austral winter–spring period (June–October) represents the well-documented BB season in South America (Thornhill et al., 2018; Rosário et al., 2022), peaking in September across Amazonia, Cerrado, and Pantanal biomes (Rosário et al., 2022).

Table 1
HYSPLIT 120-h backward-trajectory clusters at Huancayo and Rio Branco by season (2015–2021). **Note:** cluster identifiers (C1–C5) are independent at each site. Frequency is the percentage contribution to total transport. Direction is the compass bearing from the receptor to the mean trajectory origin. Distance is the great-circle distance to the trajectory origin.

		Huancayo			Rio Branco		
Season	Cluster	Freq. (%)	Dir.	Dist. (km)	Freq. (%)	Dir.	Dist. (km)
DJF	C1	59.9	ESE	132	52.9	N	316
	C2	3.3	NNE	399	7.3	NE	1192
	C3	7.8	ENE	510	1.7	NE	1216
	C4	17.8	ENE	72	15.8	NNE	919
	C5	11.1	ENE	252	22.3	N	526
MAM	C1	63.7	E	124	21.3	ESE	383
	C2	7.5	NE	132	58.2	ENE	149
	C3	2.0	W	268	6.7	SE	671
	C4	5.3	E	334	2.2	SSE	371
	C5	21.6	ENE	130	11.6	ESE	606
JJA	C1	7.6	NE	142	61.5	ESE	240
	C2	69.3	ENE	113	9.0	SSE	1180
	C3	6.6	ENE	253	3.7	S	1149
	C4	1.1	W	800	25.6	SE	984
	C5	15.4	NE	108	0.2	SW	6136
SON	C1	67.3	ESE	119	65.5	N	130
	C2	4.4	NNW	182	1.3	ESE	774
	C3	6.3	ENE	219	23.2	NE	378
	C4	20.4	ENE	141	0.3	SSW	3996
	C5	1.6	W	1114	9.7	ENE	690

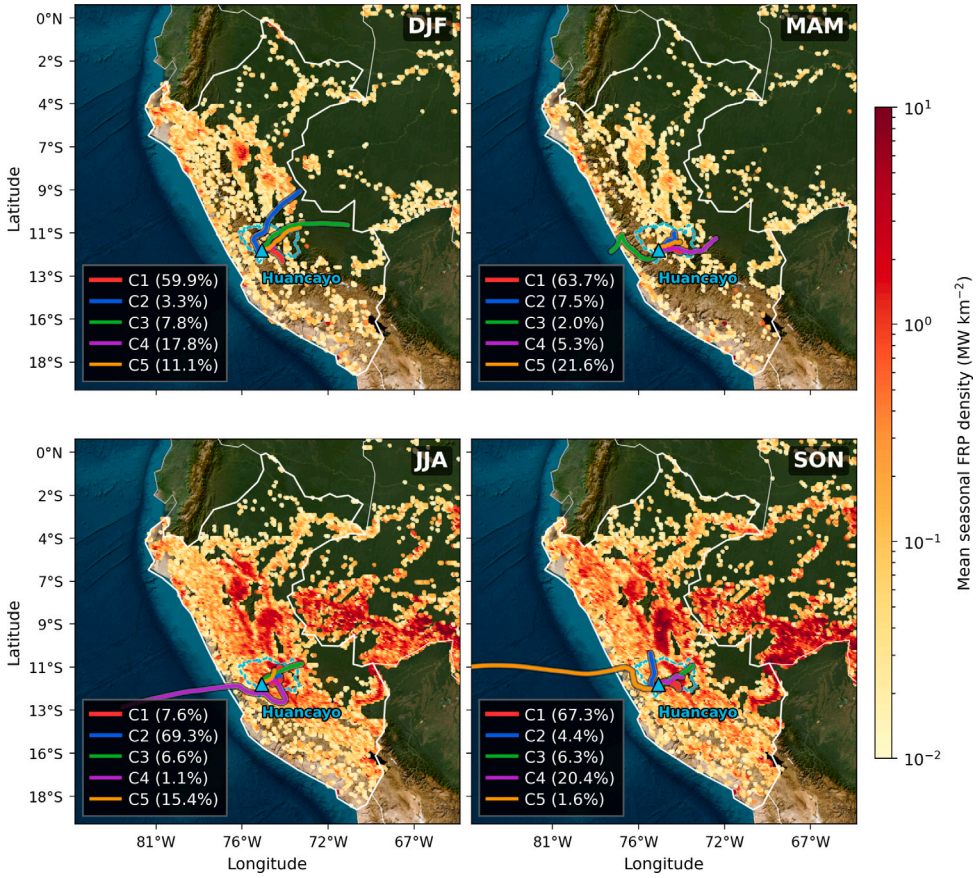

Fig. 4. Seasonal 120-hour backward trajectory clusters arriving at Huancayo Observatory for the 2015–2021 period, overlaid with mean seasonal Fire Radiative Power (FRP) density (MW km^{-2}) from VIIRS-SNPP active-fire detections.

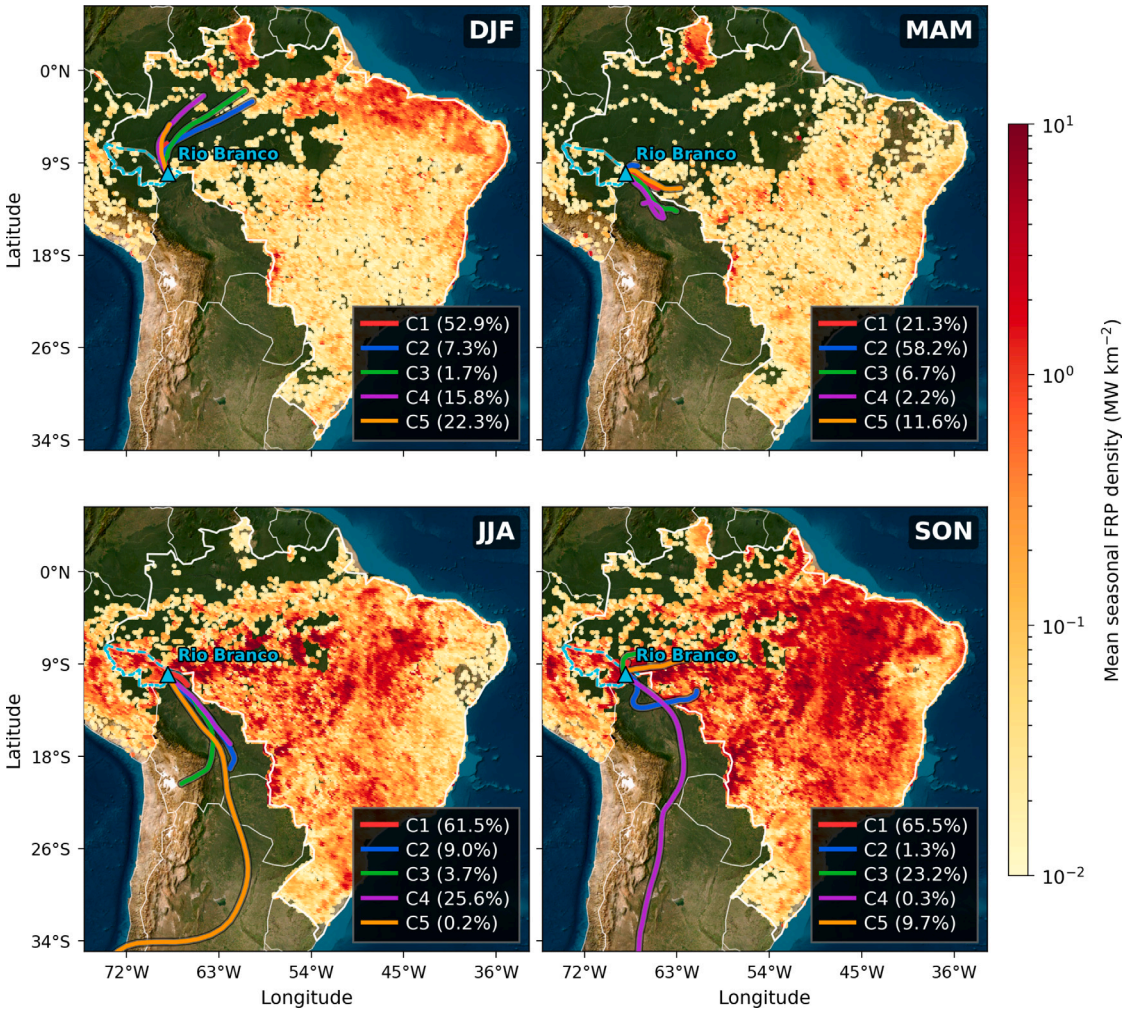

Fig. 5. Similar to Fig. 4, but for Rio Branco.

During the wet season (DJF–MAM), fire activity is virtually absent at both sites (median fire counts of 24–41), suppressed by monsoon precipitation and elevated fuel moisture. Fire–aerosol correlations are correspondingly weak at Huancayo (Table 3) but moderate at Rio Branco during DJF (AOD_{440}–Fires r = 0.49; $PM_{2.5}$–Fires r = 0.51), reflecting residual aerosols from the previous dry season transported to this lowland Amazonian site.

The dry season marks dramatic fire intensification, but with markedly different spatial patterns at each site. At Huancayo, high-density fire regions (15–20 MW km^{-2}) develop in the Peruvian Amazon lowlands east of 75°W, with median fire counts increasing from 746 in JJA to 1054 in SON. The dominant easterly clusters (C2 in JJA; C1+C4 in SON) traverse these intense fire zones at distances of 300–600 km, establishing efficient long-range transport. At Rio Branco, fire activity intensifies even more dramatically, from 1501 events in JJA to 5009 in SON (Table 2), with widespread FRP density of 10–22 MW km^{-2} surrounding the receptor in a roughly circular pattern. The dominant southeastern (JJA) and northern (SON) clusters traverse these intense local fire regions at <200 km, establishing direct, near-field exposure. Both sites exhibit strong fire–aerosol correlations during JJA–SON (regional AOD_{440}–Fires: r = 0.53–0.88; $PM_{2.5}$–Fires: r = 0.71–0.89; Table 3; see Section 3.1.2 for the regional and trajectory-weighted aggregation methods), and Rio Branco additionally shows the strongest AOD_{440}–$PM_{2.5}$ correlation of any season at either site during SON (r = 0.93), reflecting the overwhelming dominance of local BB emissions. Absolute aerosol concentrations at Rio Branco during SON (AOD_{440} = 0.315; $PM_{2.5}$ = 11.7 μg m^{-3}) more than double those at Huancayo (AOD_{440} = 0.145; $PM_{2.5}$ = 4.6 μg m^{-3}), reflecting Rio Branco's position within the core BB region.

Table 3 additionally reports trajectory-weighted fire correlations (Section 3.1.2, Eq. (1)). The trajectory-weighted approach yields stronger correlations precisely where transport direction matters most: at Huancayo during SON (r = 0.66 vs. 0.53 for AOD_{440}–Fires), where only specific cluster pathways traverse the active burning regions, and at Rio Branco during DJF (r = 0.62 vs. 0.49 for AOD_{440}–Fires; r = 0.64 vs. 0.51 for $PM_{2.5}$–Fires), when residual aerosol loading is driven by distant fires rather than local emissions. During JJA, both metrics yield comparable correlations at both sites, consistent with pervasive fire activity along essentially all trajectory directions.

The seasonal evolution demonstrates contrasting fire–aerosol regimes: median fire counts at Rio Branco amplify 209-fold from DJF (24) to SON (5009), compared to 44-fold at Huancayo (24 to 1054). Huancayo receives aerosols from distant fire sources (300–600 km east) via long-range transport during JJA–SON, whereas Rio Branco experiences direct local and near-field fire influence (<200 km) with substantially shorter transport times and higher aerosol concentrations. The peak fire activity at Rio Branco during SON (FRP density >20 MW km^{-2}) coincides with the maximum AOD_{440} (0.315) and $PM_{2.5}$ (11.7 μg m^{-3}) observed across both sites and all seasons, underscoring the severe air quality impacts of BB in the western Amazon lowlands during the late dry season. Beyond bulk fire-aerosol correlations, the temporal evolution of aerosol composition and size distribution provides direct chemical and microphysical evidence for

Table 2
Seasonal median values of AOD, Ångström exponent (AE), $PM_{2.5}$, and fire counts at Huancayo and Río Branco (2015–2021). $PM_{2.5}$ in μg m^{-3}.

	Huancayo					Río Branco				
Season	Overall	DJF	MAM	JJA	SON	Overall	DJF	MAM	JJA	SON
AOD_{440}	0.091	0.083	0.073	0.092	0.145	0.120	0.084	0.085	0.155	0.315
AOD_{870}	0.039	0.039	0.030	0.036	0.048	0.055	0.040	0.038	0.055	0.109
$AE_{440-870}$	1.398	1.299	1.351	1.410	1.519	1.252	1.063	1.104	1.621	1.580
$PM_{2.5}$	3.708	3.862	3.070	3.510	4.617	7.769	5.768	7.035	8.437	11.718
Fires	143	24	41	746	1054	192	24	31	1501	5009

Table 3
Pearson correlation coefficients (r) between AOD_{440}, $PM_{2.5}$ and fire counts by season at Huancayo and Río Branco (2015–2021). Columns show the correlations AOD_{440}–$PM_{2.5}$, AOD_{440}–Fires (regional and trajectory-weighted, Eq. (1)), $PM_{2.5}$–Fires (regional and trajectory-weighted), and AOD_{440}–AOD_{870}.

	Huancayo						Río Branco					
	AOD_{440}–PM	AOD_{440}–F		PM–F		AOD_{440}–AOD_{870}	AOD_{440}–PM	AOD_{440}–F		PM–F		AOD_{440}–AOD_{870}
Season		Reg.	Traj.	Reg.	Traj.			Reg.	Traj.	Reg.	Traj.	
DJF	0.15	−0.01	0.18	−0.01	−0.01	0.92	0.58	0.49	0.62	0.51	0.64	0.95
MAM	0.37	0.01	−0.03	−0.05	−0.03	0.93	−0.02	−0.12	0.22	0.28	0.23	0.94
JJA	0.83	0.88	0.89	0.89	0.90	0.97	0.55	0.69	0.69	0.88	0.87	0.99
SON	0.69	0.53	0.66	0.71	0.72	0.95	0.93	0.67	0.57	0.72	0.70	0.99

the contrasting regimes inferred from transport and fire activity, as examined in the next section.

4.3. Seasonal aerosol composition

To characterize the chemical composition and temporal evolution of aerosols reaching Huancayo and Rio Branco, we integrated AERONET retrievals with MERRA-2 reanalysis speciated aerosol products. Throughout this section, the following data source conventions are maintained: aerosol optical properties (AOD, single scattering albedo, Ångström exponent, asymmetry parameter, and size distributions) are derived exclusively from AERONET Level 2.0 retrievals and represent direct observations; $PM_{2.5}$ mass concentrations and speciated composition (BC, OC, dust, sulfate, sea salt) are derived from MERRA-2 reanalysis and represent model-derived estimates rather than direct measurements (see Section 2.2.3). MERRA-2 provides daily mass concentrations of five aerosol components: black carbon (BC), organic carbon (OC), dust, sulfate (SO_4^{2-}), and sea salt, enabling source attribution and seasonal composition analysis. This multi-year dataset (2015–2021) captures interannual variability driven by climate modes (ENSO), fire regime fluctuations, and long-range transport variations, providing a comprehensive assessment of aerosol loading and composition across contrasting Andean–Amazonian environments.

4.3.1. Temporal variability and composition

Fig. 6 presents the seven-year time series of AOD_{440} from AERONET and MERRA-2, alongside MERRA-2 speciated $PM_{2.5}$ components and monthly VIIRS fire detections for Huancayo. The time series reveals pronounced seasonal cycles superimposed on significant interannual variability, with distinct BB episodes recurring annually during the austral winter-spring period (gray-shaded regions, approximately June–October).

At Huancayo (Fig. 6, top panel), AOD_{440} exhibits recurring seasonal maxima during the BB season (gray-shaded periods), with peak values ranging from approximately 0.15 to 0.24 across different years. The wavelength dependence of AOD is clearly visible throughout the record, with AOD_{870} (dashed line) consistently lower than AOD_{440} (solid line), reflecting fine-mode aerosol dominance particularly during BB episodes. During the wet season (regions between gray bands), AOD_{440} drops to background levels near 0.05–0.08. The fire detection time series (orange line) shows clear annual cycles with minimal activity during wet seasons and peaks during the gray-shaded burning seasons, with maximum fire counts ranging from approximately 1000 to 4500 detections across different years, demonstrating substantial interannual variability.

The bottom panel of Fig. 6 displays the MERRA-2 $PM_{2.5}$ speciated composition. The stacked area plot shows that aerosol composition varies dramatically between seasons. During the wet seasons, $PM_{2.5}$ concentrations remain near 3–4 μg m^{-3} with relatively mixed composition visible through the multiple colored layers. During the BB seasons (gray-shaded periods), the MERRA-2-modeled total $PM_{2.5}$ increases to approximately 6–8 μg m^{-3}, with OC (green layer) becoming the dominant component and expanding to occupy the majority of the vertical space in the stacked plot. Sulfate (cyan layer) shows consistent presence throughout the record as a mid-level layer. The persistence of sulfate as a year-round, non-seasonal component of $PM_{2.5}$ at Huancayo (12%–23% of total mass; Section 4.3 composition analysis) is notable because BB emits primarily organic and elemental carbon rather than sulfate, and dust contributions are mineral. This persistent sulfate signal points to non-fire local anthropogenic sources, of which the most plausible is the La Oroya poly-metallic smelter complex located ~70 km north–northwest of Huancayo. Carn et al. (2007) reported direct OMI satellite detection of SO_2 plumes from La Oroya at ~0.07 Tg yr^{-1}, and Espinoza-Guillen et al. (2023) documented mean SO_2 concentrations of 264 μg m^{-3} at La Oroya (55% of days exceeding WHO 24-hour guideline) for the period 2018–2020, confirming that the source remains active throughout our study period. Photochemical oxidation of these emissions during transport across the Mantaro Valley is consistent with the year-round presence of sulfate aerosol observed at Huancayo, distinct from the strongly fire-modulated OC and BC components. In addition, growing artisanal gold-mining activity in the Andean–Amazonian transition zone (Madre de Dios and adjacent regions) introduces a further, less constrained source of combustion-derived BC and SO_2 via uncontrolled diesel generators, dredge engines, and amalgam burning, which deserves dedicated source apportionment in future work. Disentangling BB, mineral dust, and local mining contributions through receptor modeling and isotopic tracers represents a natural follow-on to the present study. Dust (yellow layer) appears as a persistent base layer with relatively stable contributions year-round. BC (dark gray, bottom layer) shows subtle seasonal enhancement during burning periods, though it remains a minor component. Sea salt (purple, top layer) contributions are minimal throughout the record.

The temporal correspondence between fire activity peaks and aerosol loading maxima is evident, with OC expansions in the bottom panel occurring synchronously or shortly after fire count peaks in the top panel. This coupling provides direct evidence of BB aerosol transport to Huancayo during the dry season.

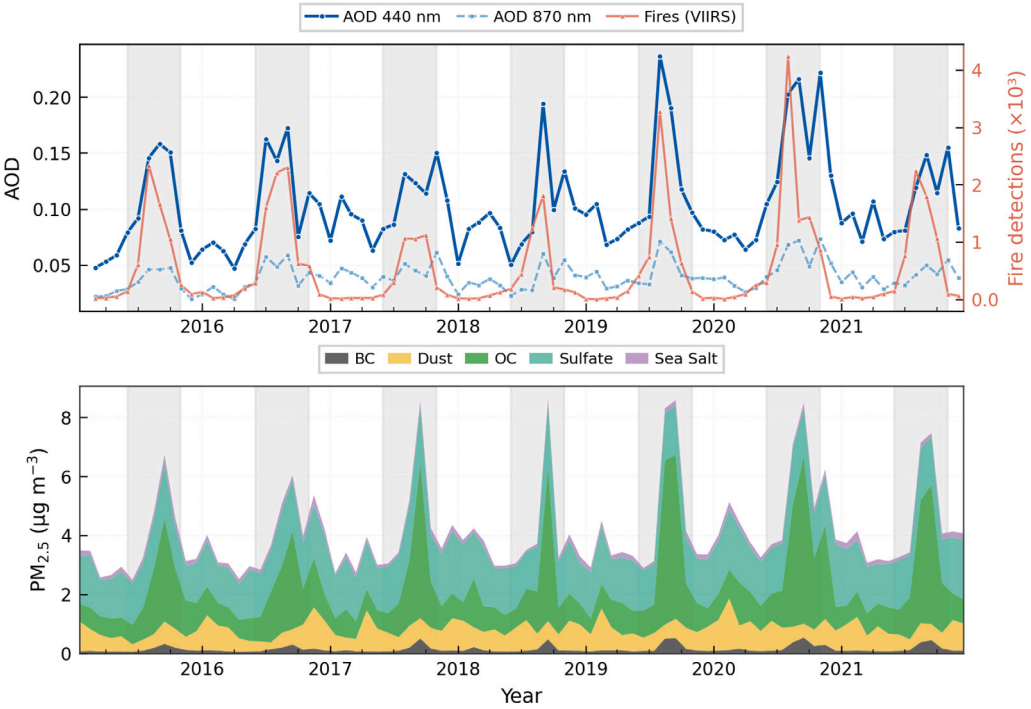

Fig. 6. Monthly mean time series (2015–2021) of (top) AOD at 440 nm (blue solid) and 870 nm (blue dashed) from AERONET with monthly VIIRS fire detections (orange), and (bottom) MERRA-2 $PM_{2.5}$ speciated components (stacked area: OC in green, sulfate in cyan, dust in yellow, BC in dark gray, and sea salt in purple) at Huancayo. Gray-shaded areas indicate the austral BB season (JJA–SON). (For interpretation of the references to color in this figure legend, the reader is referred to the web version of this article.)

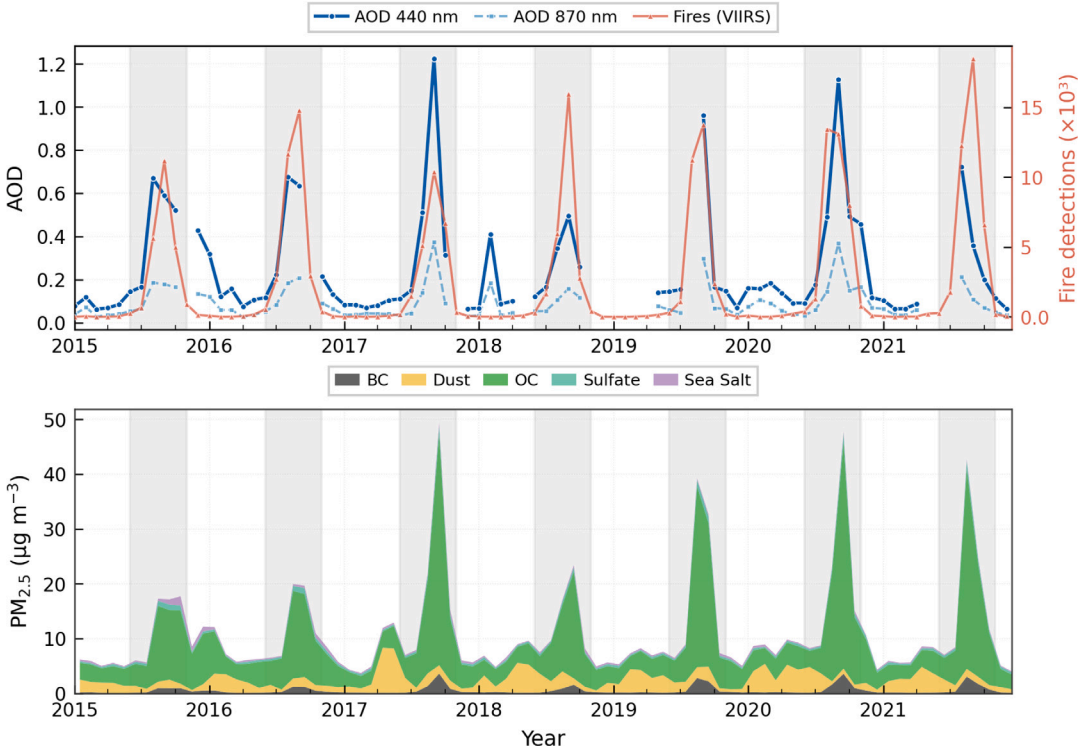

Fig. 7. Monthly mean time series (2015–2021) at Rio Branco. Top panel: AOD at 440 nm and 870 nm from AERONET with monthly VIIRS fire detections. Bottom panel: $PM_{2.5}$ speciated components. Similar to Fig. 6, but note the substantially different *y*-axis scales reflecting much higher aerosol concentrations.

Fig. 7 presents the corresponding time series for Rio Branco, revealing dramatically higher aerosol loading compared to Huancayo. The top panel shows AOD_{440} peaks exceeding 1.0 during several intense burning episodes, with the most extreme events reaching approximately 1.2. Fire detections at Rio Branco show much higher counts than Huancayo, with peak values approaching 18,000 detections during the most severe burning seasons. The contrast between wet and dry seasons is more pronounced than at Huancayo, with near-zero AOD and fire

activity during wet seasons (white regions) transitioning to extreme values during burning seasons (gray-shaded regions).

The bottom panel shows that the MERRA-2-modeled $PM_{2.5}$ composition at Rio Branco undergoes extreme seasonal transformations. During wet seasons, concentrations remain near 5–7 μg m^{-3} with relatively mixed composition visible through multiple colored layers. However, during burning seasons, total $PM_{2.5}$ increases dramatically to approximately 40–50 μg m^{-3} during the most intense events, with OC (green layer) completely dominating the composition and occupying nearly the entire vertical space in the stacked plot. The visual impression is striking: during peak burning periods, the plot becomes almost entirely green, with other components barely visible as thin layers at the base.

An notable feature is the appearance of substantial yellow (dust) layers during the late wet season and early dry season periods (visible as yellow bands in March–June of several years), particularly prominent before the onset of intense BB. This dust enhancement is more pronounced at Rio Branco than at Huancayo and represents a distinctive characteristic of the site.

BC (dark gray layer at base) shows clear seasonal enhancement during burning periods, becoming more prominent relative to other components. Sulfate (cyan) and sea salt (purple) remain minor components throughout the record, barely visible even during non-burning periods.

A notable difference between the two sites is the temporal relationship between fire activity and aerosol response. At Rio Branco, aerosol peaks occur essentially simultaneously with fire count maxima, with no discernible lag. This contrasts with Huancayo, where a slight temporal offset between fire peaks and maximum aerosol loading is sometimes apparent, consistent with longer transport times from distant sources versus near-field direct exposure at Rio Branco.

4.3.2. Aerosol size distribution characteristics

The compositional contrast documented in the previous section – OC dominance at Rio Branco vs. mixed dust/sulfate/OC at Huancayo – should manifest as distinct microphysical signatures in the aerosol size distribution, since fine-mode particles are diagnostic of combustion sources while coarse-mode particles indicate dust and sea salt contributions. Fig. 8 presents the seasonal mean aerosol volume size distributions $dV(r)/d\ln r$ derived from AERONET inversion products at both sites, revealing distinct bimodal characteristics typical of atmospheric aerosols influenced by both fine-mode (combustion) and coarse-mode (dust, sea salt) sources.

At Rio Branco (right panel), the size distributions exhibit clear bimodal structure with pronounced seasonal variations. The fine mode, centered at 0.15–0.2 μm radius, shows dramatic seasonal amplification with SON (green line) reaching approximately 2–3 times higher than DJF (red line), directly reflecting fresh combustion aerosol accumulation from widespread BB (Reid et al., 2005). The coarse mode (5–10 μm) shows slight enhancement during MAM (orange line), consistent with elevated dust mobilization from deforested areas during the wet-to-dry transition. The fine-mode peak position at 0.15–0.2 μm is characteristic of aged smoke particles that undergo coagulation and condensational growth during atmospheric transport (Reid et al., 2005). We note that the standard AERONET inversion algorithm (Dubovik and King, 2000) parameterizes the size distribution a priori as a sum of two lognormal modes (fine and coarse), so the bimodal structure described here reflects this retrieval framework rather than an independent test of modality. In principle, trimodal solutions could be derived from AERONET sky-radiance measurements through dedicated inversions with relaxed modal constraints, which represents a direction for future analysis—particularly for the broad coarse mode at Huancayo, where contributions from multiple dust source regions at different transport distances might be better resolved by a three-mode fit.

At Huancayo (left panel), the seasonal patterns differ markedly from Rio Branco. The fine mode shows maximum during SON (green line) and JJA (blue line), but with substantially lower peak heights than Rio Branco despite comparable median fire counts in upwind source regions (Table 2), suggesting aerosol dilution and deposition during long-range transport (300–600 km). The most distinctive feature is the prominent coarse mode throughout all seasons, with comparable or enhanced volume during wet seasons (DJF, MAM) relative to dry seasons. This persistent coarse-mode presence indicates substantial mineral dust influence from Altiplano, inter-Andean valleys, and Andean slope sources (Moreno et al., 2024), particularly during the convectively active wet season when strong surface winds enhance dust mobilization (Rondanelli et al., 2019).

The contrasting size distributions provide microphysical evidence for fundamentally different aerosol regimes: Rio Branco exhibits strong fine-mode seasonal amplification (threefold increase) with relatively stable coarse mode, characteristic of direct BB exposure, while Huancayo shows moderate fine-mode enhancement combined with persistent substantial coarse-mode presence year-round, characteristic of aged transported smoke mixed with regional dust. The Ångström exponent values (Table 2) corroborate these patterns, with Rio Branco showing higher median AE during burning seasons (1.58–1.62) indicating fine-mode dominance, while Huancayo displays more moderate values (1.41–1.52) reflecting mixed contributions from fine smoke and coarse dust (Reid et al., 2005; Moreno et al., 2024).

The integrated analysis reveals two fundamentally distinct aerosol regimes reflecting the interplay between source proximity, transport mechanisms, and topographic barriers in the Andean–Amazonian system. Rio Branco experiences direct, near-field exposure (< 200 km) to intense seasonal BB during June–October (Freitas et al., 2005), manifesting in extreme aerosol loading (AOD_{440} up to 1.25, $PM_{2.5}$ > 50 μg m^{-3}), zero temporal lag between fires and aerosol response, overwhelming OC dominance (> 90% during JJA–SON), and pronounced fine-mode amplification (threefold increase) with peaks at 0.15–0.2 μm characteristic of fresh BB smoke (Reid et al., 2005). In contrast, Huancayo (3313 m a.s.l.) receives diluted, aged smoke from distant fires (300–600 km east) via long-range transport, resulting in moderate aerosol loading (AOD_{440} < 0.25, $PM_{2.5}$ < 10 μg m^{-3}), observable temporal lag (2–4 weeks), and mixed composition with persistent dust (18%–30%), sulfate (12%–23%), and OC (50%–65%) contributions throughout the annual cycle, reflecting regional mineral dust influence from Altiplano and Andean sources (Moreno et al., 2024). These contrasting regimes have distinct implications: Rio Branco faces severe health-relevant $PM_{2.5}$ exposure exceeding WHO guidelines during burning seasons (Organization et al., 2021), while Huancayo's mixed aerosol population may influence Andean glacial melting through BC and dust deposition (Molina et al., 2015). Substantial interannual variability (2015–2021) with exceptional fire years (2017, 2018, 2021: AOD > 1.2 at Rio Branco) driven by drought conditions underscores the vulnerability of the Amazon–Andes system to changing fire regimes and emphasizes the need for continued long-term monitoring to understand aerosol–climate feedbacks in this critical tropical region.

4.3.3. Public health implications of seasonal $PM_{2.5}$ exposure

The compositional and microphysical contrasts documented in Sections 4.3–4.3.2 translate directly into differential human exposure burdens. At Rio Branco, median $PM_{2.5}$ concentrations during the late dry season (SON) reach 11.7 μg m^{-3} (Table 2), with episodic peaks exceeding 50 μg m^{-3} during exceptional fire years (2018, 2021), values that frequently surpass both the WHO annual guideline (5 μg m^{-3}) and the 24-hour guideline (15 μg m^{-3}) (Organization et al., 2021). Unlike isolated pollution events, these elevated concentrations persist systematically during the dry season, especially from June to October, resulting in recurrent exposure over several consecutive months each year. Under these conditions, the seasonal peaks effectively constitute a repeated chronic exposure pattern rather than short-term atmospheric anomalies.

This prolonged exposure is particularly relevant because BB aerosols at Rio Branco are dominated by OC (>90% of $PM_{2.5}$ during JJA–SON), together with BC and BrC, all of which are associated with

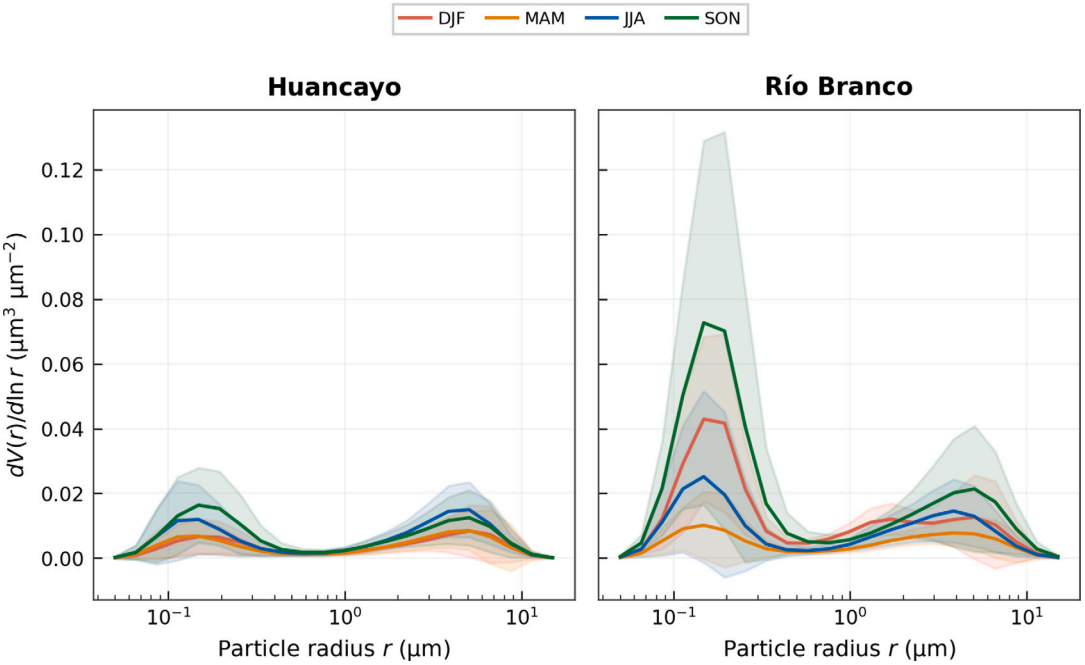

Fig. 8. Seasonal mean aerosol volume size distributions from AERONET inversion products at (left) Huancayo and (right) Rio Branco for the period 2015–2021. Shaded areas represent one standard deviation from the mean. The x-axis shows particle radius in logarithmic scale (0.1–100 μm). The bimodal distribution reveals fine-mode aerosols (0.1–0.5 μm, primarily from combustion) and coarse-mode aerosols (1–10 μm, dust and sea salt).

adverse respiratory and cardiovascular outcomes. Repeated inhalation of fine particles from biomass combustion has been linked to increased hospital admissions for asthma and bronchitis, reduced pulmonary function, ischemic cardiovascular events, and adverse outcomes in children and older adults. In the western Amazon, Coker et al. (2022) reported a significant association between daily $PM_{2.5}$ variability and respiratory hospitalizations in Rio Branco, confirming the direct health burden during the fire season. The cumulative effect of repeated dry-season exposure over successive years may further increase long-term risks, especially among children, older adults, outdoor workers, and individuals with pre-existing cardiopulmonary disease.

Although aerosol concentrations at Huancayo remain substantially lower, the mixed composition observed there – characterized by transported OC, persistent mineral dust (18%–30%), and sulfate – also represents a relevant exposure pathway. Fine and coarse particles transported across the Andean valleys may contribute to respiratory irritation, inflammatory responses, and chronic exposure to inhalable particulate matter, particularly during the dry season when regional transport intensifies and atmospheric dispersion is reduced. Furthermore, Huancayo's elevation (3313 m a.s.l.) means residents are physiologically more vulnerable to respiratory aerosol exposure relative to sea-level populations due to reduced atmospheric oxygen partial pressure.

Quantifying the total public health burden in terms of attributable mortality or disability-adjusted life years remains challenging because concentration–response functions and long-term epidemiological records are still limited across tropical South America. Nevertheless, the much stronger aerosol loading and the 2.3-fold higher atmospheric radiative forcing observed at Rio Branco compared to Huancayo (Section 4.4) indicate not only a stronger climatic impact but also a substantially greater human exposure burden. This reflects an important environmental justice dimension, where communities located closest to deforestation fronts and agricultural burning areas are disproportionately exposed to the health consequences of regional land-use change.

These findings highlight the need to strengthen continuous air-quality monitoring, expand epidemiological surveillance, and implement seasonal public health alerts during the June–October burning period. Preventive actions aimed at reducing exposure during extreme fire episodes should be integrated with land-use management and fire-control policies, particularly in the Andean–Amazonian transition zone where climate impacts and human health risks converge. Beyond these direct exposure effects, the contrasting aerosol compositions documented above – OC- and BC-rich at Rio Branco vs. mixed carbonaceous–mineral at Huancayo – also imply distinct radiative impacts, since the optical properties governing absorption and scattering depend directly on these compositional and microphysical contrasts. The following section quantifies these radiative effects.

4.4. Aerosol radiative forcing

Building on the compositional and microphysical contrasts established in the previous sections, aerosol radiative forcing (ARF) quantifies the climatic impact of aerosols, with positive values indicating atmospheric warming and negative values representing cooling (Kocifaj et al., 2025). We calculated ARF at three levels: top of atmosphere (TOA), bottom of atmosphere (BOA), and within the atmosphere (ATM), providing a comprehensive assessment of aerosol radiative effects at both receptor sites.

Fig. 9 reveals distinct seasonal patterns and dramatic site-specific differences in aerosol radiative forcing. We quantified the uncertainty associated with these estimates through a single-scattering-albedo (SSA) perturbation analysis (Supplementary Section 5, Table S3, Figure S4); reported values are accompanied by their ±0.01 SSA perturbation envelopes, which represent a physically consistent lower bound on the SSA-driven uncertainty (since larger perturbations would push some retrievals outside the physically valid range $[0, 1]$).

At Huancayo (left panel), ARF estimates are available only for the dry season (JJA and SON) when aerosol loading is sufficient for reliable forcing calculations. During SON, peak values are BOA −18.0 W m^{-2}, TOA +15.4 W m^{-2}, and ATM +33.4 W m^{-2} [27.6, 32.7] (±18%); JJA shows slightly lower values (BOA −16.3, TOA +13.5, ATM +29.8 W m^{-2} [24.3, 28.0], ±20%). The absence of ARF estimates during wet seasons reflects minimal aerosol loading when fire activity is negligible and wet deposition efficiently removes atmospheric particles. Negative BOA forcing indicates surface cooling from aerosol extinction

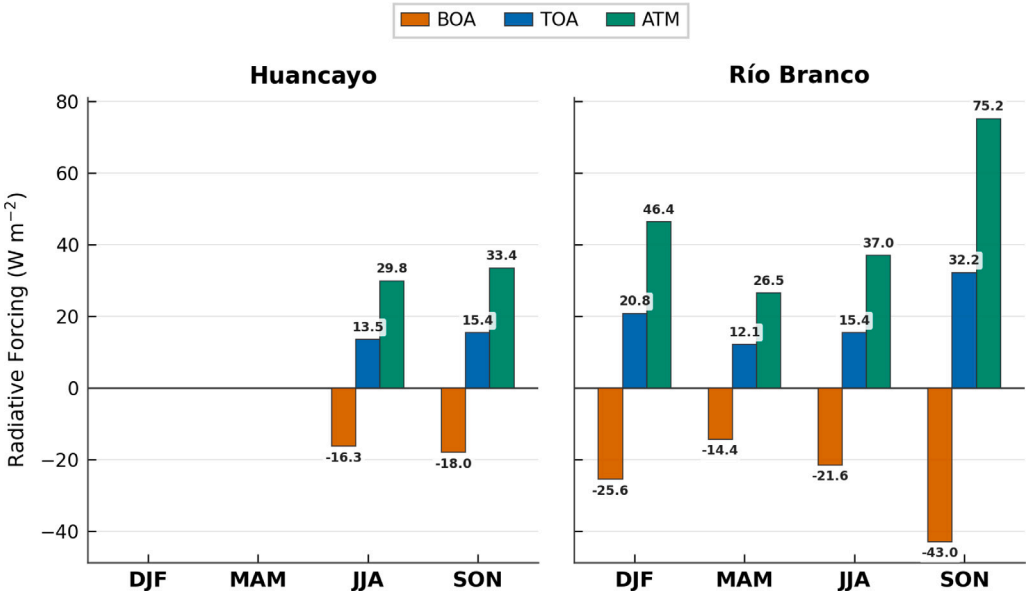

Fig. 9. Seasonal aerosol radiative forcing (ARF, W m^{-2}) at the bottom of atmosphere (BOA, orange), top of atmosphere (TOA, blue), and within the atmosphere (ATM, green) for (left) Huancayo and (right) Rio Branco during 2015–2021. Note that ARF estimates at Huancayo are only available for JJA and SON due to insufficient aerosol loading during wet seasons (DJF, MAM). (For interpretation of the references to color in this figure legend, the reader is referred to the web version of this article.)

of incoming solar radiation, while positive TOA forcing reflects atmospheric warming from backscattered radiation. The positive ATM forcing (29.8–33.4 W m^{-2}) indicates substantial atmospheric heating as absorbing aerosols trap energy within the atmospheric column, primarily driven by BC and brown carbon (BrC) from BB emissions; BC is a strong light absorber across all wavelengths, while BrC exhibits wavelength-dependent absorption with maximum efficiency in the UV and near-visible spectrum (Mok et al., 2016). The OC dominance (50%–65%) at Huancayo during JJA–SON (Fig. 6) includes significant BrC fractions that, combined with BC (4%–5%), produce mid-tropospheric warming alongside surface cooling.

At Rio Branco (right panel), ARF magnitudes are dramatically larger, particularly during BB periods. SON exhibits extreme values: BOA −43.0 W m^{-2}, TOA +32.2 W m^{-2}, and ATM +75.2 W m^{-2} [50.4, 93.7] (±33%), representing 2.1–2.4-fold enhancements compared to Huancayo during the same season. Even JJA at Rio Branco (ATM +37.0 W m^{-2} [23.9, 47.7], ±37%) exceeds Huancayo's maximum values, with the largest relative uncertainty occurring under the lowest SSA conditions where forcing is most sensitive to absorption specification. During wet seasons, Rio Branco maintains detectable forcing (DJF: ATM +46.4 W m^{-2}; MAM: ATM +26.5 W m^{-2}), indicating persistent aerosol presence from residual smoke and local dust sources, contrasting with Huancayo's negligible wet-season aerosol loading. The Rio Branco surface forcing values reported here (−43 W m^{-2} during SON) fall within the range of −21 to −74 W m^{-2} documented by Procopio et al. (2004) from a multi-year AERONET-based analysis at heavily fire-impacted Amazonian sites, while the atmospheric heating values (+37 to +75 W m^{-2} during JJA–SON) lie at the high end of their reported 3–30 W m^{-2} range, reflecting Rio Branco's position within the most intensely impacted southwestern Amazon. The consistency of our magnitudes with this independent multi-year Amazonian baseline reinforces confidence in the inter-site contrast quantified here.

The extreme atmospheric heating at Rio Branco during SON results from the overwhelming dominance of fresh BB emissions (>90% OC), which include both strongly absorbing BC (5%–6% of $PM_{2.5}$) and substantial BrC fractions within the OC component. Mok et al. (2016) retrieved the column-effective imaginary refractive index (k) for Amazonian BB aerosols using AERONET inversions during the Bolivian dry-season campaign and showed enhanced k values in the UV (305–368 nm) attributable to BrC absorption, with diminished values in the visible–NIR consistent with BC-dominated absorption at longer wavelengths—a spectral signature characteristic of the OC-rich regime observed at Rio Branco during JJA–SON. The combined absorption by BC and BrC produces the "heat trapping" configuration evident in our results, where surface cooling (negative BOA) occurs simultaneously with mid-tropospheric warming (positive ATM), reducing the surface-to-atmosphere temperature gradient. This vertical heating profile is physically consistent with mechanisms of atmospheric stability modification, convection suppression, and reduced precipitation documented in modeling studies of Amazonian BB (Zhang et al., 2020; Li et al., 2022), although the quantitative attribution of such feedbacks at the specific sites studied here would require dedicated regional climate modeling beyond the scope of this observational analysis.

The site-specific differences in atmospheric radiative forcing extend beyond differences in aerosol loading (AOD_{440}: 0.315 vs. 0.145, Table 2) and are amplified by contrasting aerosol optical properties driven by emission age and composition. AERONET inversion retrievals indicate that at Rio Branco during peak burning season (SON), single scattering albedo at 440 nm (SSA_{440}) ranges from 0.93 to 0.95, consistent with values reported for fresh Amazonian BB smoke (Pérez-Ramírez et al., 2017). These SSA values reflect substantial light absorption relative to scattering, driven by high BC and BrC concentrations in fresh primary combustion aerosols emitted from local fires within <200 km. In contrast, Huancayo exhibits slightly higher SSA_{440} values during JJA–SON, reflecting the mixed composition of aged smoke transported over 300–600 km combined with strongly scattering mineral dust (18%–30% of $PM_{2.5}$ from MERRA-2, Section 4.3). Aging during transport produces partial photochemical bleaching of BrC and oxidative loss of OC, while non-absorbing mineral dust further reduces bulk absorption efficiency. This contrast in SSA explains why the inter-site difference in atmospheric forcing efficiency (ARF per unit AOD) amplifies the raw AOD difference: Rio Branco's lower SSA produces disproportionately higher atmospheric absorption per unit optical depth than Huancayo's mixed scattering–absorbing aerosol population, contributing to the 2.3-fold inter-site contrast in atmospheric radiative forcing beyond what AOD differences alone would predict.

To place the aerosol regimes documented here within a broader global context, the contrasting Andean–Amazonian forcing magnitudes

can be compared with values reported for other major aerosol systems worldwide. The atmospheric forcing at Rio Branco during SON (+75.2 W m^{-2}) is among the highest reported for BB environments globally, exceeding values from Asian megacity absorbing aerosol campaigns (+10 to +30 W m^{-2}, Nakajima et al. 2007) and global biomass-burning radiative forcing estimates (~68 mW m^{-2} on a globally averaged basis when integrated over all biomass and fossil burning sources, Jiang et al. 2022), reflecting the local-scale intensity of Amazonian dry-season fire emissions. Long-range transport of fire emissions producing optically thick aerosol layers has also been documented at intercontinental scales, as recently reported for the 2023 Canadian wildfires reaching southern Europe (Filonchyk and Peterson, 2024)—a phenomenon analogous in mechanism, though smaller in magnitude than the Amazon-to-Andes transport documented in this study. In contrast, dust-dominated systems such as the 2023 Asian sand and dust storm events over China generated PM_{10} concentrations exceeding 1,000 μg m^{-3} and $AOD_{550} > 1$ (Filonchyk et al., 2024), but with substantially lower absorption efficiency than carbonaceous aerosols, illustrating that fresh BB aerosols can produce stronger atmospheric heating per unit AOD than mineral dust due to their higher imaginary refractive index. Episodic stratospheric perturbations from the 2021 Mt. Etna eruptions (Sellitto et al., 2022b) and the 2022 Hunga Tonga–Hunga Ha'apai eruption (Sellitto et al., 2022a) produce radiative forcing through entirely different mechanisms (sulfate and water vapor injection in the stratosphere) but reinforce the broader principle that aerosol composition, vertical distribution, and source proximity together determine radiative impact. The Andean–Amazonian contrast documented here – a 2.3-fold difference in atmospheric forcing between sites separated by topography rather than emission source – illustrates a process distinct from these other regimes: the role of orographic barriers in modulating both aerosol loading and composition, with implications generalizable to other tropical mountain–lowland systems globally.

These results demonstrate that aerosol climatic impacts are substantially more pronounced in the lowland Amazon compared to the high Andes, with SON atmospheric radiative forcing differing by a factor of 2.3 between sites. This disparity reflects differences in both aerosol loading (AOD_{440} 0.315 vs. 0.145, Table 2) and composition, with Rio Branco's fresh BB smoke containing higher mass fractions of strongly absorbing carbonaceous aerosols. The cumulative radiative forcing from BB aerosols represents a significant perturbation to the regional energy budget with potential consequences for Amazonian climate stability and Andean cryosphere dynamics.

5. Conclusions

We investigated aerosol transport, composition, optical properties, and radiative forcing at two contrasting receptor sites in tropical South America during 2015–2021: Huancayo Observatory (12.04° S, 75.32° W, 3313 m a.s.l.) in the central Peruvian Andes and Rio Branco (9.96° S, 67.87° W, 212 m a.s.l.) in the southwestern Brazilian Amazon. By integrating AERONET sun photometer observations, VIIRS-SNPP active fire detections, HYSPLIT backward trajectories, and MERRA-2 speciated aerosol products, we provide the first systematic comparative characterization of aerosol regimes across the Andean–Amazonian transition zone, building on the single-site framework of Victoria-Barros and Estevan Arredondo (2025).

The trajectory analysis revealed fundamentally distinct transport regimes. Huancayo receives east-northeasterly trajectories during the dry season (67%–69% of cases) traversing intense fire regions 300–600 km east, with transit times of 3–5 days, while Rio Branco experiences direct, near-field exposure (<200 km) to local biomass burning emissions, with dominant southeastern trajectories during JJA (87%) intersecting the most active fire zones. Fire activity amplifies 44-fold from DJF to SON at Huancayo and 209-fold at Rio Branco, reflecting Rio Branco's position within the core Amazonian burning region.

The two sites display fundamentally different aerosol regimes. Rio Branco is dominated by OC (>90% of $PM_{2.5}$) during JJA–SON, with extreme aerosol loading (AOD_{440} up to 1.25; $PM_{2.5}$ exceeding 50 μg m^{-3} during exceptional fire years 2018 and 2021) and zero temporal lag between fires and aerosol response. Huancayo receives diluted, aged smoke (2–4 week lag) with mixed composition: dust (18%–30%), sulfate (12%–23%), and OC (50%–65%). The persistent year-round sulfate fraction at Huancayo, distinct from the strongly fire-modulated OC and BC components, is attributable primarily to the La Oroya poly-metallic smelter (~70 km NE; Carn et al. 2007) and potentially to artisanal mining activity, identifying the Andean component of the transition zone as a multi-source receptor in which biomass burning operates alongside persistent local industrial emissions.

Aerosol size distributions and radiative forcing reflect these compositional contrasts. Rio Branco exhibits pronounced fine-mode amplification (threefold from wet to dry season) consistent with fresh smoke, while Huancayo displays moderate fine-mode enhancement combined with year-round coarse-mode presence (5–10 μm) reflecting Altiplano and Andean dust sources. Aerosol radiative forcing differs by a factor of 2.3 between sites during SON (Huancayo ATM +33.4 W m^{-2} [27.6, 32.7]; Rio Branco ATM +75.2 W m^{-2} [50.4, 93.7], with ±0.01 SSA perturbation envelopes from Supplementary Section 5). The contrast is robust across the full uncertainty range, driven by both higher aerosol loading at Rio Branco and lower SSA from absorbing BC and BrC in fresh combustion aerosols, producing a "heat trapping" configuration where surface cooling coincides with mid-tropospheric warming.

These contrasting regimes have distinct consequences. Rio Branco experiences severe health-relevant $PM_{2.5}$ exposure far exceeding WHO air quality guidelines (annual mean: 5 μg m^{-3}; 24-hour mean: 15 μg m^{-3}) during the burning season, while Huancayo's mixed aerosol population may influence Andean glacial melting through BC and dust deposition. Substantial interannual variability across the seven-year record reveals exceptional fire years (2017–2021) driven by drought conditions, underscoring the vulnerability of the Andean–Amazonian system to changing fire regimes.

Future research priorities include: (i) expansion of ground-based monitoring networks (AERONET, lidar, in-situ samplers) to improve spatial coverage and validate remote sensing and reanalysis products; (ii) vertical profiling of aerosol optical properties to reduce uncertainty in radiative forcing estimates; (iii) source apportionment combined with chemical transport modeling to quantify contributions from biomass burning, biogenic emissions, mineral dust, and local industrial sources (e.g., La Oroya smelter, artisanal mining); (iv) spectral characterization of absorbing aerosols (BC and BrC) across UV–visible wavelengths; and (v) investigation of aerosol–cloud–precipitation interactions to quantify indirect radiative effects and potential feedbacks between atmospheric heating, convection suppression, and drought conditions that may exacerbate fire regimes in the Amazon–Andes region.

CRediT authorship contribution statement

Cesar Victoria-Barros: Writing – original draft, Validation, Software, Methodology, Investigation, Funding acquisition, Formal analysis, Data curation, Conceptualization. **René Estevan:** Writing – original draft, Methodology, Data curation, Conceptualization. **Octavio Fashé Raymundo:** Writing – original draft, Project administration, Funding acquisition. **Héctor Navarro-Barboza:** Writing – review & editing, Supervision, Software, Methodology, Investigation.

Declaration of competing interest

The authors declare that they have no known competing financial interests or personal relationships that could have appeared to influence the work reported in this paper.

Acknowledgments

This research was supported by the Universidad Nacional Mayor de San Marcos, Republic of Peru through resolution RR N° 005446-2025-R/UNMSM and project number B25132231.

The authors acknowledge NASA for providing AERONET data and maintaining the Huancayo and Rio Branco observation sites. We thank the AERONET principal investigators and site managers for their efforts in establishing and maintaining the stations used in this study. VIIRS active fire data were obtained from NASA's Fire Information for Resource Management System (FIRMS). MERRA-2 reanalysis data were provided by the Global Modeling and Assimilation Office (GMAO) at NASA Goddard Space Flight Center through the NASA GES DISC. Meteorological data for HYSPLIT trajectory calculations were provided by NOAA's Air Resources Laboratory.

We are grateful to the HYSPLIT and SBDART development teams for making their models freely available to the scientific community. The authors thank Yahweh Tayta for his valuable technical support during this research.

Appendix A. Supplementary data

Supplementary material related to this article can be found online at https://doi.org/10.1016/j.envint.2026.110340.

Data availability

All data used in this study are publicly available. AERONET aerosol optical depth and inversion products (Version 3.0, Level 2.0) are available at https://aeronet.gsfc.nasa.gov/. VIIRS-SNPP active fire data are distributed through NASA's Fire Information for Resource Management System (FIRMS) at https://firms.modaps.eosdis.nasa.gov/. MERRA-2 reanalysis products are accessible through NASA's Goddard Earth Sciences Data and Information Services Center (GES DISC) at https://disc.gsfc.nasa.gov/. GDAS meteorological data are provided by NOAA's Air Resources Laboratory at https://www.ready.noaa.gov/. The HYSPLIT model is freely available at https://www.ready.noaa.gov/HYSPLIT.php, and SBDART radiative transfer code can be obtained from https://paulricchiazzi.com/www/sbdart/. Processed data and analysis scripts used in this study are available from the corresponding author upon reasonable request.

References

Artaxo, P., Rizzo, L.V., Brito, J.F., Barbosa, H.M.J., Arana, A., Sena, E.T., Cirino, G.G., Bastos, W., Martin, S.T., Andreae, M.O., 2013. Atmospheric aerosols in amazonia and land use change: from natural biogenic to biomass burning conditions. Faraday Discuss. 165, 203–235.

Bolaño-Truyol, J., Schneider, I.L., Cuadro, H.C., Bolaño-Truyol, J.D., Oliveira, M.L., 2022. Estimation of the impact of biomass burning based on regional transport of PM2. 5 in the Colombian caribbean. Geosci. Front. 13 (1), 101152.

Boucher, O., Randall, D., Artaxo, P., Bretherton, C., Feingold, G., Forster, P., Kerminen, V.-M., Kondo, Y., Liao, H., Lohmann, U., et al., 2013. Clouds and aerosols. In: Climate Change 2013: The Physical Science Basis. Contribution of Working Group I To the Fifth Assessment Report of the Intergovernmental Panel on Climate Change. Cambridge University Press, pp. 571–657.

Buchard, V., et al., 2017. The MERRA-2 aerosol reanalysis, 1980 onward. Part II: Evaluation and case studies. J. Clim. 30 (17), 6851–6872. http://dx.doi.org/10.1175/JCLI-D-16-0613.1.

Carn, S.A., Krueger, A.J., Krotkov, N.A., Yang, K., Levelt, P.F., 2007. Sulfur dioxide emissions from Peruvian copper smelters detected by the Ozone Monitoring Instrument. Geophys. Res. Lett. 34, L09801. http://dx.doi.org/10.1029/2006GL029020.

Coker, E.S., Buralli, R., Manrique, A.F., Kanai, C.M., Amegah, A.K., Gouveia, N., 2022. Association between PM2. 5 and respiratory hospitalization in rio branco, Brazil: Demonstrating the potential of low-cost air quality sensor for epidemiologic research.. Environ. Res. 214, 113738.

Dehkhoda, N., Shin, J., Joo, S., Sim, J., Noh, Y., 2024. An AERONET-based methodology to retrieve black carbon light absorption and comparison with MERRA-2 data. Atmospheric Pollut. Res. 15 (2), 101994.

Dorling, S., Davies, T., Pierce, C., 1992. Cluster analysis: A technique for estimating the synoptic meteorological controls on air and precipitation chemistry—Method and applications. Atmospheric Environ. Part A. Gen. Top. 26 (14), 2575–2581.

Draxler, R.R., Hess, G., 1998. An overview of the hysplit_4 modelling system for trajectories. Aust. Meteorol. Mag. 47 (4), 295–308.

Draxler, R.R., Spayd, L.E., 1999. HYSPLIT radiological transport and dispersion model implementation on NCEP cray. Citeseer.

Dubovik, O., King, M.D., 2000. A flexible inversion algorithm for retrieval of aerosol optical properties from Sun and sky radiance measurements. J. Geophys. Res. 105 (D16), 20673–20696. http://dx.doi.org/10.1029/2000JD900282.

Eck, T.F., Holben, B., Reid, J., Dubovik, O., Smirnov, A., O'neill, N., Slutsker, I., Kinne, S., 1999. Wavelength dependence of the optical depth of biomass burning, urban, and desert dust aerosols. J. Geophys. Res.: Atmospheres 104 (D24), 31333–31349.

Espinoza, J.C., Chavez, S., Ronchail, J., Junquas, C., Takahashi, K., Lavado, W., 2015. Rainfall hotspots over the southern tropical andes: Spatial distribution, rainfall intensity, and relations with large-scale atmospheric circulation. Water Resour. Res. 51 (5), 3459–3475. http://dx.doi.org/10.1002/2014WR016273, URL: https://agupubs.onlinelibrary.wiley.com/doi/abs/10.1002/2014WR016273.

Espinoza-Guillen, J.A., Alderete-Malpartida, M.B., Cañari-Cancho, J.H., Pando-Huerta, D.L., Vargas-La Rosa, D.F., Bernabé-Meza, S.J., 2023. Immission levels and identification of sulfur dioxide sources in La Oroya city, Peruvian Andes. Environ. Dev. Sustain. 25 (11), 12843–12872. http://dx.doi.org/10.1007/s10668-022-02592-0.

Estevan, R., Martínez-Castro, D., Suarez-Salas, L., Moya, A., Silva, Y., 2019. First two and a half years of aerosol measurements with an aeronet sunphotometer at the huancayo observatory, peru. Atmospheric Environ.: X (ISSN: 2590-1621) 3, 100037. http://dx.doi.org/10.1016/j.aeaoa.2019.100037, URL: https://www.sciencedirect.com/science/article/pii/S2590162119300395.

Faisal, S.I., Islam, M.S., 2026. Modeling and validation of airborne effluent dispersion and radiological doses from a VVER-1200 reactor routine operations using HYSPLIT. Ann. Nucl. Energy 227, 111986.

Filonchyk, M., Peterson, M.P., 2024. Changes in aerosol properties at the el arenosillo site in southern europe as a result of the 2023 Canadian forest fires. Environ. Res. 260, 119629. http://dx.doi.org/10.1016/j.envres.2024.119629.

Filonchyk, M., Peterson, M.P., Zhang, L., Yan, H., 2024. An analysis of air pollution associated with the 2023 sand and dust storms over China: Aerosol properties and PM_{10} variability. Geosci. Front. 15 (2), 101762. http://dx.doi.org/10.1016/j.gsf.2023.101762.

Freitas, S.R., Longo, K.M., Silva Dias, M.A., Silva Dias, P.L., Chatfield, R., Prins, E., Artaxo, P., Grell, G.A., Recuero, F.S., 2005. Monitoring the transport of biomass burning emissions in south america. Environ. Fluid Mech. 5 (1), 135–167.

Garreaud, R.D., Vuille, M., Compagnucci, R., Marengo, J., 2009. Present-day south american climate. Palaeogeogr. Palaeoclimatol. Palaeoecol. 281 (3–4), 180–195.

Gelaro, R., McCarty, W., Suárez, M.J., Todling, R., Molod, A., Takacs, L., Randles, C.A., Darmenov, A., Bosilovich, M.G., Reichle, R., et al., 2017. The modern-era retrospective analysis for research and applications, version 2 (MERRA-2). J. Clim. 30 (14), 5419–5454. http://dx.doi.org/10.1175/JCLI-D-16-0758.1.

Giles, D.M., Sinyuk, A., Sorokin, M.G., Schafer, J.S., Smirnov, A., Slutsker, I., Eck, T.F., Holben, B.N., Lewis, J.R., Campbell, J.R., et al., 2019. Advancements in the aerosol robotic network (AERONET) version 3 database–automated near-real-time quality control algorithm with improved cloud screening for sun photometer aerosol optical depth (AOD) measurements. Atmospheric Meas. Tech. 12 (1), 169–209.

Holben, B.N., Eck, T.F., Slutsker, I.a., Tanre, D., Buis, J., Setzer, A., Vermote, E., Reagan, J.A., Kaufman, Y., Nakajima, T., et al., 1998. AERONET—A federated instrument network and data archive for aerosol characterization. Remote Sens. Environ. 66 (1), 1–16.

Jiang, K., Fu, B., Luo, Z., Xiong, R., Men, Y., Shen, H., Li, B., Shen, G., Tao, S., 2022. Attributed radiative forcing of air pollutants from biomass and fossil burning emissions. Environ. Pollut. 306, 119378. http://dx.doi.org/10.1016/j.envpol.2022.119378.

Kalkstein, L.S., Tan, G., Skindlov, J.A., 1987. An evaluation of three clustering procedures for use in synoptic climatological classification. J. Appl. Meteorol. Clim. 26 (6), 717–730.

Kocifaj, M., Kundracik, F., Gueymard, C., 2025. Radiative warming by multicomponent soot-dominated aerosols can be controlled by material configuration. Environ. Int. 197, 109343.

Legg, S., 2021. IPCC, 2021: Climate change 2021-the physical science basis. Interaction 49 (4), 44–45.

Li, J., Carlson, B.E., Yung, Y.L., Lv, D., Hansen, J., Penner, J.E., Liao, H., Ramaswamy, V., Kahn, R.A., Zhang, P., et al., 2022. Scattering and absorbing aerosols in the climate system. Nat. Rev. Earth Environ. 3 (6), 363–379.

Ma, X., Yu, F., 2014. Seasonal variability of aerosol vertical profiles over east US and west europe: GEOS-chem/APM simulation and comparison with CALIPSO observations. Atmos. Res. (ISSN: 0169-8095) 140–141, 28–37. http://dx.doi.org/10.1016/j.atmosres.2014.01.001, URL: https://www.sciencedirect.com/science/article/pii/S0169809514000027.

Marengo, J.A., Soares, W.R., Saulo, C., Nicolini, M., 2004. Climatology of the low-level jet east of the andes as derived from the NCEP–NCAR reanalyses: Characteristics and temporal variability. J. Clim. 17 (12), 2261–2280.

Mendez-Espinosa, J., Belalcazar, L., Betancourt, R.M., 2019. Regional air quality impact of northern south america biomass burning emissions. Atmos. Environ. 203, 131–140.

Mok, J., Krotkov, N.A., Arola, A., Torres, O., Jethva, H., Andrade, M., Labow, G., Eck, T.F., Li, Z., Dickerson, R.R., Stenchikov, G.L., Osipov, S., Ren, X., 2016. Impacts of brown carbon from biomass burning on surface UV and ozone photochemistry in the Amazon Basin. Sci. Rep. 6, 36940. http://dx.doi.org/10.1038/srep36940.

Molina, L.T., Gallardo, L., Andrade, M., Baumgardner, D., Borbor-Córdova, M., Bórquez, R., Casassa, G., Cereceda-Balic, F., Dawidowski, L., Garreaud, R., et al., 2015. Pollution and its impacts on the south American cryosphere. Earth's Futur. 3 (12), 345–369.

Moran-Zuloaga, D., Ditas, F., Walter, D., Saturno, J., Brito, J., Carbone, S., Chi, X., Hrabě de Angelis, I., Baars, H., Godoi, R.H.M., Heese, B., Holanda, B.A., Lavrič, J.V., Martin, S.T., Ming, J., Pöhlker, M.L., Ruckteschler, N., Su, H., Wang, Y., Wang, Q., Wang, Z., Weber, B., Wolff, S., Artaxo, P., Pöschl, U., Andreae, M.O., Pöhlker, C., 2018. Long-term study on coarse mode aerosols in the amazon rain forest with the frequent intrusion of saharan dust plumes. Atmospheric Chem. Phys. 18 (13), 10055–10088.

Moreno, C.I., Krejci, R., Jaffrezo, J.-L., Uzu, G., Alastuey, A., Andrade, M.F., Mardóñez, V., Koenig, A.M., Aliaga, D., Mohr, C., et al., 2024. Tropical tropospheric aerosol sources and chemical composition observed at high altitude in the bolivian andes. Atmospheric Chem. Phys. 24 (5), 2837–2860.

Myhre, G., Shindell, D., Bréon, F.-M., Collins, W., Fuglestvedt, J., Huang, J., Koch, D., Lamarque, J.-F., Lee, D., Mendoza, B., Nakajima, T., Robock, A., Stephens, G., Takemura, T., Zhang, H., 2013. Anthropogenic and natural radiative forcing. In: Clim. Chang. 2013: Phys. Sci. Basis 659–740.

Nakajima, T., Yoon, S.-C., Ramanathan, V., Shi, G.-Y., Takemura, T., Higurashi, A., Takamura, T., Aoki, K., Sohn, B.-J., Kim, S.-W., et al., 2007. Overview of the atmospheric brown cloud east Asian regional experiment 2005 and a study of the aerosol direct radiative forcing in east Asia. J. Geophys. Res.: Atmospheres 112 (D24).

National Centers for Environmental Prediction, National Weather Service, NOAA, U.S. Department of Commerce, 2000. NCEP FNL Operational Model Global Tropospheric Analyses, continuing from July 1999. NSF National Center for Atmospheric Research, Boulder, CO, http://dx.doi.org/10.5065/D6M043C6, URL: https://doi.org/10.5065/D6M043C6.

Navarro-Barboza, H., Moya-Álvarez, A., Luna, A., Fashé-Raymundo, O., 2020. Influence evaluation of PM10 produced by the burning of biomass in peru on AOD, using the WRF-chem. Atmósfera 33 (1), 71–86.

Navarro-Barboza, H., Rovira, J., Obiso, V., Pozzer, A., Via, M., Alastuey, A., Querol, X., Perez, N., Savadkoohi, M., Chen, G., et al., 2025. Characterization of brown carbon absorption in different European environments through source contribution analysis. Atmospheric Chem. Phys. 25 (4), 2667–2694.

Organization, W.H., et al., 2021. WHO global air quality guidelines: particulate matter (PM2. 5 and PM10), ozone, nitrogen dioxide, sulfur dioxide and carbon monoxide. World Health Organization.

Palacios-Peña, L., Jiménez-Guerrero, P., Baró, R., Balzarini, A., Bianconi, R., Curci, G., Landi, T.C., Pirovano, G., Prank, M., Riccio, A., Tuccella, P., Galmarini, S., 2019. Aerosol optical properties over europe: an evaluation of the aqmeii phase 3 simulations against satellite observations. Atmospheric Chem. Phys. 19 (5), 2965–2990. http://dx.doi.org/10.5194/acp-19-2965-2019, URL: https://acp.copernicus.org/articles/19/2965/2019/.

Pérez-Ramírez, D., Andrade-Flores, M., Eck, T.F., Stein, A.F., O'Neill, N.T., Lyamani, H., Gassó, S., Whiteman, D.N., Veselovskii, I., Velarde, F., Alados-Arboledas, L., 2017. Multi year aerosol characterization in the tropical andes and in adjacent amazonia using AERONET measurements. Atmos. Environ. (ISSN: 1352-2310) 166, 412–432. http://dx.doi.org/10.1016/j.atmosenv.2017.07.037, URL: https://www.sciencedirect.com/science/article/pii/S1352231017304788.

Procopio, A.S., Artaxo, P., Kaufman, Y.J., Remer, L.A., Schafer, J.S., Holben, B.N., 2004. Multiyear analysis of Amazonian biomass burning smoke radiative forcing of climate. Geophys. Res. Lett. 31 (3), http://dx.doi.org/10.1029/2003GL018646, L03108.

Rai, M., Mahapatra, P.S., Gul, C., Kayastha, R.B., Panday, A.K., Puppala, S.P., 2019. Aerosol radiative forcing estimation over a remote high-altitude location (˜ 4900 masl) near yala glacier, nepal. Aerosol Air Qual. Res. 19 (8), 1872–1891.

Randles, C.A., da Silva, A.M., Buchard, V., Colarco, P.R., Darmenov, A., Govindaraju, R., Smirnov, A., Holben, B., Ferrare, R., Hair, J., et al., 2017. The MERRA-2 aerosol reanalysis, 1980 onward. Part I: System description and data assimilation evaluation. J. Clim. 30 (17), 6823–6850. http://dx.doi.org/10.1175/JCLI-D-16-0609.1.

Reid, J.S., Eck, T.F., Christopher, S.A., Koppmann, R., Dubovik, O., Eleuterio, D.P., Holben, B.N., Reid, E.A., Zhang, J., 2005. A review of biomass burning emissions part III: intensive optical properties of biomass burning particles. Atmospheric Chem. Phys. 5, 827–849. http://dx.doi.org/10.5194/acp-5-827-2005.

Ricchiazzi, P., Yang, S., Gautier, C., Sowle, D., 1998. SBDART: A research and teaching software tool for plane-parallel radiative transfer in the earth's atmosphere. Bull. Am. Meteorol. Soc. 79 (10), 2101–2114.

Rolph, G., Stein, A., Stunder, B., 2017. Real-time environmental applications and display system: READY. Environ. Model. Softw. 95, 210–228.

Rondanelli, R., Hatchett, B., Rutllant, J., Bozkurt, D., Garreaud, R., 2019. Strongest MJO on record triggers extreme atacama rainfall and warmth in antarctica. Geophys. Res. Lett. 46 (6), 3482–3491.

Rosário, N.E.D., Sena, E.T., Yamasoe, M.A., 2022. South American 2020 regional smoke plume: intercomparison with previous years, impact on solar radiation, and the role of pantanal biomass burning season. Atmospheric Chem. Phys. 22 (22), 15021–15033. http://dx.doi.org/10.5194/acp-22-15021-2022, URL: https://acp.copernicus.org/articles/22/15021/2022/.

Rosas Santana, J., Lima da Silva, G., Akemi Yamasoe, M., Èvora do Rosario, N., 2025. Biomass burning smoke transport and radiative impact over the city of são paulo: an extreme event case study. Atmospheric Chem. Phys. 25 (22), 15935–15951.

Sangura, M.T., Althaf, P., Makokha, J.W., Boiyo, R., Kumar, K.R., 2025. Estimation and model performance of aerosol radiative forcing from radiative transfer models using the AERONET data over Kenya, east africa. Adv. Space Res. 75 (1), 481–496.

Schroeder, W., Oliva, P., Giglio, L., Csiszar, I.A., 2014. The new VIIRS 375 m active fire detection data product: Algorithm description and initial assessment. Remote Sens. Environ. 143, 85–96. http://dx.doi.org/10.1016/j.rse.2013.12.008.

Sellitto, P., Podglajen, A., Belhadji, R., et al., 2022a. The unexpected radiative impact of the Hunga Tonga eruption of 15 January 2022. Commun. Earth Environ. 3, 288. http://dx.doi.org/10.1038/s43247-022-00618-z.

Sellitto, P., et al., 2022b. Volcanic emissions, plume dispersion, and downwind radiative impacts following Mount Etna series of eruptions of February 21–26, 2021. J. Geophys. Res.: Atmospheres 127, http://dx.doi.org/10.1029/2021JD035974, e2021JD035974.

Sena, E., Artaxo, P., Correia, A., 2012. The impact of deforestation in the amazonian atmospheric radiative balance: a remote sensing assessment.. Atmospheric Chem. Phys. Discuss. 12 (6).

Sena, E.T., Artaxo, P., Correia, A.L., 2013. Spatial variability of the direct radiative forcing of biomass burning aerosols and the effects of land use change in amazonia. Atmospheric Chem. Phys. 13 (3), 1261–1275.

Stamnes, K., Tsay, S.-C., Wiscombe, W., Jayaweera, K., 1988. Numerically stable algorithm for discrete-ordinate-method radiative transfer in multiple scattering and emitting layered media. Appl. Opt. 27 (12), 2502–2509.

Stein, A.F., Draxler, R.R., Rolph, G.D., Stunder, B.J., Cohen, M.D., Ngan, F., 2015. Noaa's HYSPLIT atmospheric transport and dispersion modeling system. Bull. Am. Meteorol. Soc. 96 (12), 2059–2077.

Stohl, A., 1998. Computation, accuracy and applications of trajectories—A review and bibliography. Atmos. Environ. 32 (6), 947–966.

Thornhill, G.D., Ryder, C.L., Highwood, E.J., Shaffrey, L.C., Johnson, B.T., 2018. The effect of south American biomass burning aerosol emissions on the regional climate. Atmospheric Chem. Phys. 18 (8), 5321–5342. http://dx.doi.org/10.5194/acp-18-5321-2018, URL: https://acp.copernicus.org/articles/18/5321/2018/.

Uribe-Ventura, R., Barriga-Berrios, Y., Barriga-Gamarra, J., Baby, P., Viveen, W., 2025. AI-based geological subsurface reconstruction using sparse convolutional autoencoders. Comput. Geosci. 105981.

Victoria, C., Estevan, R., 2021. Comportamiento de los aerosoles atmosféricos en el observatorio de huancayo durante los eventos de quema de biomasa del año 2019. Rev. de Investigación de FíSica 24 (1), 40–54. http://dx.doi.org/10.15381/rif.v24i1.20246, URL: https://doi.org/10.15381/rif.v24i1.20246.

Victoria-Barros, C., Estevan Arredondo, R., 2025. Characterization of the optical properties of biomass-burning aerosols in two high andean cities, huancayo and la paz, and their effect on radiative forcing. Atmosphere (ISSN: 2073-4433) 16 (11), http://dx.doi.org/10.3390/atmos16111240, URL: https://www.mdpi.com/2073-4433/16/11/1240.

Zhang, X., et al., 2020. Modeling the global radiative effect of brown carbon. Atmospheric Chem. Phys. 20, 1901–1920. http://dx.doi.org/10.5194/acp-20-1901-2020.